MARCH 05 2026

Graphics processing unit accelerated Helmholtz equation solver in two dimensions using the traditional Born series formulation for linear and nonlinear media in biomedical ultrasound

Ujjal Mandal; Jagpreet Singh; Ben T. Cox; Ratan K. Saha

J. Acoust. Soc. Am. 159, 1948–1962 (2026)
https://doi.org/10.1121/10.0042817

JASA ARTICLE

Graphics processing unit accelerated Helmholtz equation solver in two dimensions using the traditional Born series formulation for linear and nonlinear media in biomedical ultrasound

Ujjal Mandal,[1] Jagpreet Singh,[2] Ben T. Cox,[3] and Ratan K. Saha[1,a)]
[1]Department of Applied Sciences, Indian Institute of Information Technology Allahabad, Jhalwa, Prayagraj 211015, Uttar Pradesh, India
[2]Department of Computer Science and Engineering, Indian Institute of Technology Ropar, Street 29, Ropar 140001, Punjab, India
[3]Department of Medical Physics and Biomedical Engineering, University College London, Gower Street, London WC1E 6BT, United Kingdom

ABSTRACT:
This study numerically solves inhomogeneous Helmholtz equations modeling acoustic wave propagation in homogeneous and lossless, absorbing and dispersive, and inhomogeneous and nonlinear media. The traditional Born series (TBS) method has been employed to solve such equations. Simulated pressure field patterns for a linear array of acoustic sources (a line source) estimated by the TBS procedure exhibit excellent agreement with that of a standard time domain approach (the K-WAVE toolbox). For instance, the maximum absolute error of normalized pressure amplitude made by the proposed technique for the homogeneous and lossless medium is $\approx 2\%$ with respect to the latter method. The TBS scheme, though iterative, is a very fast method. For example, the graphics processing unit (GPU)-enabled CUDA C code implementing the TBS procedure for calculating the pressure field for the homogeneous and lossless medium is $102\times$ faster than the K-WAVE module and also $4\times$ faster than the corresponding central processing unit C code for the computational domain considered in this study (4096×4096). The findings of this study demonstrate the effectiveness of the TBS method for solving inhomogeneous Helmholtz equation, while the GPU-based implementation significantly reduces the computation time. In this work, the capability and performance of the method have been tested in two dimensions only.
https://doi.org/10.1121/10.0042817

(Received 18 August 2025; revised 9 February 2026; accepted 11 February 2026; published online 5 March 2026)
[Editor: Didier Dragna] Pages: 1948–1962

I. INTRODUCTION

Ultrasound (US) imaging is a very popular medical imaging modality because it is cheap, portable, noninvasive, and nonionizing (Wang *et al.*, 2020). However, it can provide images of deeply seated soft tissue structures (penetration depth is about 6 cm for a 5 MHz transducer). Accurate determination of the pressure field emitted by a transducer is of profound importance for system design, image reconstruction, understanding wave-medium interactions, tissue characterization, development of beamforming algorithms, dosimetry for high intensity focused US therapy, and training of ultrasonographers (who use US equipment, generate and interpret images) (Gu and Jing, 2015). Different variants of time-dependent inhomogeneous wave equations are available that model acoustic wave propagation in real tissue. In general, such an equation is solved numerically to yield the pressure field distribution for a given set of initial and boundary conditions (van Manen *et al.*, 2005). An ideal simulator should (i) accommodate various transducer geometries (single element, multi-element, linear, curved, and phased array transducers), (ii) provide faithful solutions for realistic (homogeneous and lossless, absorbing and dispersive, and inhomogeneous and nonlinear) media, and (iii) handle a large computational domain and perform fast calculations for long travel time (e.g., a 6 cm distance corresponds to 200 and 400 wavelengths at 5 and 10 MHz, respectively).

The full wave equation is available in the literature, which models propagation of acoustic waves in a nonlinear, heterogeneous, and absorbing medium (Jing and Cleveland, 2007; Pinton *et al.*, 2011). For many realistic problems, a simple version, known as the Westervelt equation, can be derived. When backward-propagating waves are negligible, a one-way formulation of the Westervelt equation may be used, in which only forward-propagating components of the acoustic field are retained while preserving the full wave dispersion relation. Under an additional paraxial (narrow-angle) assumption on diffraction, this one-way Westervelt formulation further reduces to the Khokhlov–Zabolotskaya–Kuznetsov (KZK) equation, where the hemispherical dispersion relation is approximated by a paraboloidal surface. Pinton *et al.* (2011) solved the full wave equation using the finite difference method in the time domain. The KZK equation and one-way formulations of the Westervelt equation have been solved by many groups using operator-splitting

[a)]Email: ratank.saha@iiita.ac.in

and related numerical techniques (Jing and Cleveland, 2007; Varslot and Taraldsen, 2005; Zemp *et al.*, 2003). The iterative nonlinear contrast source (INCS) method reformulates the nonlinear Westervelt equation into an integral equation framework, offering high-fidelity modeling of complex scattering and inhomogeneous media with higher computational cost (Demi *et al.*, 2010; Verweij and Huijssen, 2009). The computational methodology is termed as the iterative Neumann scheme. Another well accepted simulation software is the K-WAVE toolbox, where the *k*-space pseudospectral method is implemented (Treeby and Cox, 2010a). This methodology can take care of various transducer geometries, as well as linear and nonlinear features of the propagating medium, and facilitates reliable estimates of pressure field patterns. However, as expected, the computational cost of K-WAVE grows significantly with domain size and simulation duration, particularly in three-dimensional (3D) settings.

For linear media, the Green's function method has been widely utilized to solve time-dependent wave equations. For example, the FIELD II software calculates the spatial impulse response of a transducer based on the Green's function approach (Jensen, 1991). The Rayleigh integral has also been carried out to estimate the field distribution of a transducer of interest (Wu *et al.*, 2022). These methods perform satisfactorily for homogeneous and lossless tissue media. Numerical solutions, using finite element and finite difference time domains, of wave equations involving fractional Laplacian operators for lossy media have been explored (Chen and Holm, 2004).

The broadband generalized angular spectrum method (BBGASM) is a powerful frequency domain approach for simulating nonlinear acoustic wave propagation in ultrasound applications. BBGASM enables fast and efficient broadband simulations with accuracy for multi-harmonic fields and is effective when graphics processing unit (GPU) accelerated (Varray *et al.*, 2011; Varray *et al.*, 2013). Exploring the frequency domain approach, a toolbox referred to as SIMUS, has been developed (Garcia and Varray, 2024).

For reproducibility and broader accessibility, an open source tool such as MSOUND has been developed, providing user-friendly simulation environments for both linear and nonlinear acoustic propagation in heterogeneous media (Gu and Jing, 2021). Computations are conducted in the time domain as well as the frequency domain (mixed-domain solver). Recently, deep learning methods have been explored to solve elastic/acoustic wave equations in various contexts (Sai Ganesh *et al.*, 2022; Mehtaj and Banerjee, 2025; Veerababu and Ghosh, 2025). Exploiting the above-mentioned methods, several open source simulators have been developed. A useful comparison is shown in Table I of Gu and Jing (2021).

Another approach is to convert the time-dependent wave equation into the frequency domain via the Fourier transformation technique and solve that equation to obtain the steady state field. The time-independent form is called the Helmholtz equation. The Helmholtz equation arises in many fields (Krebes, 2019; Morse and Feshbach, 1953). For example, the time-independent Schrödinger equation, describing the scattering process of a plane wave by a potential (a region with dimension on the order of the incident wavelength having slightly different material properties with respect to the ambient medium), essentially reduces to the inhomogeneous Helmholtz equation. Solving an inhomogeneous Helmholtz equation is not a trivial task. The Green's function approach is generally applied to solve such an equation expressing the total field as the sum of incident and scattered fields; it is an integral equation and is referred to as the Lippmann–Schwinger equation in quantum mechanics (Morse and Feshbach, 1953). In this formulation, the field inside the scatterer has to be known *a priori*, which is impossible to obtain and thus poses a challenge in practice. Max Born developed a method in 1926, while studying quantum scattering problems, to overcome this problem (Born, 1926). In this approach, the full wave solution is evaluated by iteratively applying the potential to the free space solution (i.e., in the absence of the scatterer/perturbation). The solution appears as an infinite series and referred to as the traditional Born series (TBS)—also, called the method of successive approximations. The first term of the series is called the first Born approximation. Higher-order terms facilitate increasingly accurate approximations to the total wave solution.

The TBS algorithm works well when the scatterer is small and weak. Recently, Osnabrugge *et al.* (2016) developed a method that is called the convergent Born series (CBS). The CBS scheme introduces a preconditioner in the TBS expression and thus extends the validity domain of the TBS protocol (Krüger *et al.*, 2017; Osnabrugge *et al.*, 2016). It provides accurate results for arbitrarily large and strong scatterers. Both the TBS and CBS schemes have been applied for photoacoustic field calculations by single cell and tissue, mimicking various practical conditions (Kaushik *et al.*, 2020; Saha, 2020, 2021; Mandal *et al.*, 2025). To the best of our knowledge, transducer pressure field calculation in inhomogeneous, absorptive, and nonlinear media reflecting realistic tissue properties using the TBS method along with GPU implementation has never been conducted. This is the novelty of the work.

The primary objective of this study is to develop and validate an efficient and fast numerical framework for simulating spatial distribution of pressure amplitude and phase produced by a linear array of point acoustic sources resembling an US transducer in two dimensions (i.e., a line source). Four types of tissue media were considered in this work: homogeneous and lossless, absorbing and dispersive, inhomogeneous (with scatterers), and nonlinear media. The corresponding inhomogeneous Helmholtz equation in two dimensions was solved by employing the TBS method (each case at a time). GPU-enabled CUDA C codes were written and executed for this purpose. The same pressure fields were also generated using the K-WAVE package for comparison. The TBS scheme is a very fast method and offers accurate estimations of the pressure field for realistic media. It is found that the TBS approach is ~77× faster than the k-wave method. The TBS technique can be developed further to determine the pressure fields produced by typical diagnostic linear and phased array transducers (3D). The main contributions of this work are (i) casting inhomogeneous Helmholtz equations (modeling acoustic wave propagation in realistic media) in terms of source and potential terms so that the TBS method can be deployed (in particular, solving a nonlinear wave equation using coupled Helmholtz equations exploiting the same framework) and (ii) GPU implementation of the TBS formulas for rapid calculations of pressure fields.

The layout of the paper is as follows. The governing equations for pressure wave propagation through various media, the Born series technique, and iterative solutions utilizing this framework for different scenarios are covered in Sec. II. Section III illustrates the computational methods and parameters considered in this study. Section IV presents the numerical results. Discussion and conclusions of this work are outlined in Secs. V and VI.

II. MODEL EQUATIONS

A. Wave equations in realistic media

1. Lossless medium

The linear wave equation for a lossless homogeneous medium is given by (Morse and Feshbach, 1953)

$$\nabla^2 p(\mathbf{r},t) - \frac{1}{v_f^2}\frac{\partial^2 p(\mathbf{r},t)}{\partial t^2} = 0, \tag{1}$$

where $p(\mathbf{r},t)$ is the space-time-dependent acoustic pressure with $\mathbf{r} \in \mathbb{R}^n$, $n = 1, 2, 3$, and $t \in \mathbb{R}^+$; v_f is the speed of sound for the propagating medium, and the subscript f indicates the ambient fluid medium. Note that the region of interest does not include any active acoustic source. The frequency domain equation becomes (Morse and Feshbach, 1953)

$$\nabla^2 \tilde{p}(\mathbf{r}) + k_f^2 \tilde{p}(\mathbf{r}) = 0, \tag{2}$$

where k_f is the wave number. Equation (2) represents a homogeneous Helmholtz equation, which can readily be solved for simple geometries such as an infinite plane, infinite cylinder, sphere using the method of separation of variables and applying appropriate boundary conditions. For example, there are 11 coordinate systems, where the Helmholtz equation is separable (Morse and Feshbach, 1953).

2. Absorbing and dispersive medium

It has been experimentally shown that acoustic attenuation in biological tissue is frequency dependent and can be mathematically modeled as (Hill *et al.*, 2004)

$$\alpha = \alpha_0 \omega^\nu, \tag{3}$$

where α_0 is the attenuation coefficient in Np $(\mathrm{rad/s})^{-\nu}\,\mathrm{m}^{-1}$, and it is a medium-dependent parameter, ω is the angular frequency, and ν is the power-law exponent ($\nu \neq 1$). Its typical range is $\nu \in [0, 2]$ for biological tissue (Treeby and Cox, 2010b). One corresponding time-dependent wave equation for a homogeneous but absorbing and dispersive medium can be written as (Treeby and Cox, 2010b)

$$\nabla^2 p(\mathbf{r},t) - \frac{1}{v_f^2}\frac{\partial^2}{\partial t^2}p(\mathbf{r},t) + \tau\frac{\partial}{\partial t}(-\nabla^2)^{\nu/2}p(\mathbf{r},t) + \eta(-\nabla^2)^{(\nu+1)/2}p(\mathbf{r},t) = 0, \tag{4}$$

where $\tau = -2\alpha_0 v_f^{\nu-1}$ and $\eta = 2\alpha_0 v_f^\nu \tan(\pi\nu/2)$ are two proportionality constants. The third and fourth terms on the left-hand side, displaying fractional derivative operators, account for power law absorption and associated dispersion, respectively. A fractional derivative is a generalization of the classical derivative to non-integer order, allowing the operator to represent memory effects in viscoelastic media such as soft tissue. In the frequency domain, this operator is most conveniently defined (presented later) (Treeby and Cox, 2010b). Moreover, the absorption and dispersion are interconnected via the Kramers–Kronig relations. These formulas demonstrate that the real and imaginary parts of a complex analytic function are linked to each other. It is a great tool to obtain dispersion property of a tissue if attenuation for the same is known (since frequency dependent absorption of a tissue can be easily determined experimentally) (O'Donnell *et al.*, 1981). Furthermore, these operators are together termed as the fractional Laplacian (L_{frac}):

$$L_{frac} = \tau\frac{\partial}{\partial t}(-\nabla^2)^{\nu/2} + \eta(-\nabla^2)^{(\nu+1)/2}. \tag{5}$$

The first term on the right-hand side of Eq. (5) is called the lossy operator. A generalized version of the fractional Laplacian can be written as

$$L_{frac} = \tau\frac{\partial^{2+g}}{\partial t^{2+g}}(-\nabla^2)^h + \eta\frac{\partial^{2+q}}{\partial t^{2+q}}(-\nabla^2)^w. \tag{6}$$

A particular combination of constants g, h, q, and w can be used to fit known absorption and dispersion laws, and examples are shown in Table I.

The time-independent wave equation for the same medium can be derived as

$$\nabla^2\tilde{p}(\mathbf{r}) + k_f^2\tilde{p}(\mathbf{r}) + \Big\{-i\tau\omega(-\nabla^2)^{\nu/2} + \eta(-\nabla^2)^{(\nu+1)/2}\Big\}\tilde{p}(\mathbf{r}) = 0. \tag{7}$$

TABLE I. Lossy and dispersive derivative operators (Treeby and Cox, 2010b).

Name	g	h	q	w	Dependence
Damped	-1	0	0	0	ω^0
Blackstock	1	0	0	0	ω^2
Szabo	$\nu-1$	0	0	0	ω^ν
Stokes	-1	1	0	0	ω^2
Caputo and Wismer	$\nu-3$	1	0	0	ω^ν
Chen and Holm	-1	$\nu/2$	0	0	k^ν
Treeby and Cox	-1	$\nu/2$	-2	$(\nu+1)/2$	k^ν

https://doi.org/10.1121/10.0042817

The Green's function method can be applied to solve the above equation (Treeby and Cox, 2011).

3. Inhomogeneous medium

Consider that a spherical region of radius a exists within the computational domain. The speed of sound and density of this region differ from those of the surrounding medium. The inhomogeneous region will cause scattering of the impinging wave. The time-dependent wave equation can be cast as (Morse and Ingard, 1968; Sharma and Saha, 2004; Saha and Sharma, 2005)

$$\nabla^2 p(\mathbf{r},t) - \frac{1}{v_f^2}\frac{\partial^2}{\partial t^2}p(\mathbf{r},t) = \frac{1}{v_f^2}\gamma_\kappa(\mathbf{r},t)\frac{\partial^2}{\partial t^2}p(\mathbf{r},t) + \nabla\cdot\left[\gamma_\rho(\mathbf{r},t)\nabla p(\mathbf{r},t)\right], \tag{8}$$

where

$$\gamma_\kappa(\mathbf{r},t) = \frac{\kappa_s(\mathbf{r},t)-\kappa_f}{\kappa_f}, \qquad \gamma_\rho(\mathbf{r},t) = \frac{\rho_s(\mathbf{r},t)-\rho_f}{\rho_s(\mathbf{r},t)} \tag{9}$$

inside the scattering region and $\gamma_\kappa(\mathbf{r},t) = \gamma_\rho(\mathbf{r},t) = 0$ outside the scatterer. The ρ_f and κ_f notations state the density and compressibility of the ambient medium, whereas the same quantities for the scatterer are denoted by ρ_s and κ_s, respectively. The subscript s denotes the scattering region. For $\rho_s \approx \rho_f$, Eq. (8) in the frequency domain can be approximated as

$$\nabla^2\tilde{p}(\mathbf{r}) + k_f^2\tilde{p}\Big(\mathbf{r}\Big) = \begin{cases} -(k_s^2-k_f^2)\tilde{p}(\mathbf{r}), \\ 0, \end{cases} \tag{10}$$

for inside and ourside of the scatterer, respectively. As stated above, exact solutions of Eq. (10) can be deduced for regular shapes by imposing continuity of pressure and normal component of the particle velocity on the surface of the inhomogeneity (Colton and Kress, 1998; Morse and Ingard, 1968; Saha, 2007)

4. Nonlinear medium

The time-dependent wave equation for a nonlinear medium yields (Hamilton and Blackstock, 1998)

$$\nabla^2 p(\mathbf{r},t) - \frac{1}{c_0^2}\frac{\partial^2 p(\mathbf{r},t)}{\partial t^2} + \xi\frac{\partial^2 p^2(\mathbf{r},t)}{\partial t^2} = -S(\mathbf{r})\cos(\omega t), \tag{11}$$

$$\text{where} \quad \xi = \frac{1}{\rho_f v_f^4}\left(1+\frac{1}{2}\frac{B}{A}\right),$$

and B/A is called the nonlinearity parameter, which characterizes the relative contribution of finite-amplitude effects to the sound speed (Hamilton and Blackstock, 1998). The above equation closely resembles the non-absorbing Westervelt equation (Hamilton and Blackstock, 1998). The acoustic source is a real-valued sinusoidally varying function of time having an angular frequency ω; it attains maximum amplitude at $t = 0$. It could be expressed using the sine function as well (or in terms of complex sinusoidal functions) (Kaltenbacher, 2021; Thoens-Zueva *et al.*, 2017). The third term on the left-hand side is responsible for production of harmonics. In other words, the pressure field retains harmonics at multiples of the source frequency due to nonlinear wave propagation. Therefore, the pressure field, utilizing the method of ansatz and for the above driving function, can be expanded in terms of the Fourier series as $p(\mathbf{r},t) = \sum_{n=1}^{\infty}\mathcal{A}_n(\mathbf{r})\cos(n\omega t)$, where $\mathcal{A}_n(\mathbf{r})$ is the spatially varying complex amplitude for the n-th harmonic, providing the following coupled Helmholtz equations for the first five harmonics (Kaltenbacher, 2021),

$$\nabla^2\mathcal{A}_1 + k_1^2\mathcal{A}_1 = -S\Big(\mathbf{r}\Big) + \xi(1\omega)^2\sum_{n=1}^{\infty}\mathcal{A}_n^*\mathcal{A}_{n+1}, \tag{12a}$$

$$\nabla^2\mathcal{A}_2 + k_2^2\mathcal{A}_2 = \xi(2\omega)^2\left[\frac{1}{2}\mathcal{A}_1\mathcal{A}_1 + \sum_{n=1}^{\infty}\mathcal{A}_n^*\mathcal{A}_{n+2}\right], \tag{12b}$$

$$\nabla^2\mathcal{A}_3 + k_3^2\mathcal{A}_3 = \xi(3\omega)^2\left[\mathcal{A}_1\mathcal{A}_2 + \sum_{n=1}^{\infty}\mathcal{A}_n^*\mathcal{A}_{n+3}\right], \tag{12c}$$

$$\nabla^2\mathcal{A}_4 + k_4^2\mathcal{A}_4 = \xi(4\omega)^2\left[\frac{1}{2}\mathcal{A}_2\mathcal{A}_2 + \mathcal{A}_1\mathcal{A}_3 + \sum_{n=1}^{\infty}\mathcal{A}_n^*\mathcal{A}_{n+4}\right] \tag{12d}$$

$$\nabla^2\mathcal{A}_5 + k_5^2\mathcal{A}_5 = \xi(5\omega)^2\left[\mathcal{A}_2\mathcal{A}_3 + \mathcal{A}_1\mathcal{A}_4 + \sum_{n=1}^{\infty}\mathcal{A}_n^*\mathcal{A}_{n+5}\right], \tag{12e}$$

where the superscript $*$ indicates the complex conjugate of a field. Equation (12a) represents the wave propagation for the fundamental frequency. Equations (12b)–(12e) describe wave propagation for the 2nd–5th harmonics, respectively. The terms on the right-hand side of Eq. (12) containing complex conjugates of the pressure fields are called the difference terms; the rest are designated as the sum terms. A difference term has a frequency that is the difference between the frequencies of the components it arose from, a sum term has a frequency that is the sum of the frequencies of the components it arose from. The sum terms typically dominate, to the extent that difference terms are often neglected in practice. In other words, the accuracy of the field calculation can be improved by increasing the number of difference terms. Moreover, the field strength decreases as the frequency increases. This is because $1/n$ dependence corresponds to the asymptotic behavior in shock-forming regimes, and in quasi-linear regimes the harmonic amplitudes may deviate significantly from this scaling, and also, frequency-dependent absorption greatly reduces the amplitudes for higher harmonics in reality (Hamilton and Blackstock, 1998).

B. Derivation of the Born series

The general form of the Helmholtz equation in the presence of source terms for a lossless medium can be written as (Osnabrugge *et al.*, 2016)

$$\nabla^2\tilde{p}(\mathbf{r}) + k_f^2\tilde{p}(\mathbf{r}) = -S(\mathbf{r}) - U(\mathbf{r})\tilde{p}(\mathbf{r}), \tag{13}$$

where k_f is the wave number, S is a source term causing acoustic emission and its magnitude controls the amplitude of the pressure field, and U is the potential term appearing because of mismatch of acoustic properties of the region of interest with respect to the surrounding medium or for other factors such absorption and dispersion etc. For example, $U = k_s^2 - k_f^2$ if speed of sound mismatch exists in the propagating medium. The above equation can also be cast as (Osnabrugge *et al.*, 2016)

$$\nabla^2\tilde{p}(\mathbf{r}) + (k_f^2 + i\epsilon)\tilde{p}(\mathbf{r}) = -S(\mathbf{r}) - V(\mathbf{r})\tilde{p}(\mathbf{r}), \tag{14}$$

with $V(\mathbf{r}) = U(\mathbf{r}) - i\epsilon$, ϵ being a real positive number. The choice of ϵ depends on inhomogeneity magnitude. In Eq. (14), the propagating medium has been artificially made as an attenuating medium. However, the same attenuation factor has been included in the potential term, which amplifies the field compensating the attenuation effect. The solution to Eq. (14) can be obtained as (Morse and Feshbach, 1953)

$$\tilde{p}(\mathbf{r}) = \int g(\mathbf{r}|\mathbf{r}_0)[V(\mathbf{r}_0)\tilde{p}(\mathbf{r}_0) + S(\mathbf{r}_0)]d^3\mathbf{r}_0, \tag{15}$$

where $g(\mathbf{r}|\mathbf{r}_0)$ is the Green's function that satisfies the following equation:

$$\nabla^2 g(\mathbf{r}|\mathbf{r}_0) + (k_f^2 + i\epsilon)g(\mathbf{r}|\mathbf{r}_0) = -\delta(\mathbf{r} - \mathbf{r}_0). \tag{16}$$

Here, $\delta(\mathbf{r} - \mathbf{r}_0)$ is the Dirac delta function; the functional forms of the Green's functions in two dimensions and three dimensions can be found in the literature (Arfken *et al.*, 1995). Green's functions in the far field in two and three dimensions for lossy unbounded medium are given by Arfken *et al*. (1995), Morse and Feshbach (1953), and Saha (2020, 2021),

$$g(\mathbf{r}|\mathbf{r}_0) \approx \frac{i}{4}\left(\frac{2}{\pi\sqrt{k_f^2 + i\epsilon}|\mathbf{r}|}\right)^{1/2} e^{i\left(\sqrt{k_f^2+i\epsilon}|\mathbf{r}-\mathbf{r}_0| - (\pi/4)\right)} \tag{17}$$

and

$$g(\mathbf{r}|\mathbf{r}_0) \approx \frac{e^{i\sqrt{k_f^2+i\epsilon}|\mathbf{r}-\mathbf{r}_0|}}{4\pi|\mathbf{r}|}, \tag{18}$$

respectively. It may be mentioned that $g(\mathbf{r}|\mathbf{r}_0)$ essentially provides the field at point $\mathbf{r}$ due to a source point located at $\mathbf{r}_0$ and the field strength decreases due to natural geometrical spreading and, in addition, undergoes an artificial exponential decay introduced by the finite ϵ parameter. This renders the Green's function lossy, with the result that the total energy of the Green's function becomes finite and localized. Thus, the Fourier transform of g *vis-á-vis* $\tilde{p}$ can be calculated. In other words, the introduction of ϵ in Eq. (14) helps to evaluate the field in a finite computational domain. Equation (15) involves convolution sums and hence can be represented as

$$\tilde{p} = GV\tilde{p} + GS, \tag{19}$$

where $G = \mathcal{F}^{-1}\tilde{g}(\mathbf{K})\mathcal{F}$; $\mathcal{F}$ and $\mathcal{F}^{-1}$ are the forward and inverse Fourier transform operators, respectively, and $\tilde{g}(\mathbf{K})$ is the Fourier transform of $g(\mathbf{r}|\mathbf{r}_0)$ and is given by

$$\tilde{g}(\mathbf{K}) = \frac{1}{(|\mathbf{K}|^2 - k_f^2 - i\epsilon)}, \tag{20}$$

with $\mathcal{K}$ as the Fourier transformed coordinates. Eq. (19) can be recursively expanded, yielding

$$\tilde{p} = [1 + GV + GVGV + \cdots]GS. \tag{21}$$

Equation (21) is known as the TBS and it converges if the spectral norm of $|GV| < 1$ (Osnabrugge *et al.*, 2016). In other words, the infinite series converges for small objects with weak scattering potentials. The infinite sum in Eq. (21) can be carried out in the following manner:

$$\tilde{p}^{l+1}(\mathbf{r}) = \mathcal{F}^{-1}\left[\tilde{g}(\mathbf{K})\mathcal{F}\left[V(\mathbf{r})\tilde{p}^{l}(\mathbf{r}) + S(\mathbf{r})\right]\right]. \tag{22}$$

Therefore, the field at the $(l+1)$-th iteration is calculated using that of the l-th step. The field at the 0-th iteration can be estimated as

$$\tilde{p}^{0}(\mathbf{r}) = \mathcal{F}^{-1}[\tilde{g}(\mathbf{K})\mathcal{F}[S(\mathbf{r})]]. \tag{23}$$

It will act as the input to Eq. (22), and the field would be computed successively as the iteration progresses.

C. Solutions to the wave equations using the Born series method

1. Wave propagation through a homogeneous and lossless medium

Equation (2) after a minor modification becomes [or putting $U(\mathbf{r}) = 0$ in Eq. (14)]

$$\nabla^2\tilde{p}(\mathbf{r}) + (k_f^2 + i\epsilon)\tilde{p}(\mathbf{r}) = -S(\mathbf{r}) + i\epsilon\tilde{p}(\mathbf{r}). \tag{24}$$

Here, the $S(\mathbf{r})$ term is introduced because the region of interest retains an acoustic source (e.g., transducer elements). The solution to Eq. (24) in terms of the TBS method appears as

$$\tilde{p}^{l+1}(\mathbf{r}) = \mathcal{F}^{-1}\left[\tilde{g}(\mathbf{K})\mathcal{F}\left[-i\epsilon\tilde{p}^{l}(\mathbf{r}) + S(\mathbf{r})\right]\right], \tag{25}$$

with $V(\mathbf{r}) = -i\epsilon$. All multiplications have to be performed element wise. Equation (25) has been realized in this work to calculate the acoustic field generated by a collection of point transducer-elements.

2. Wave propagation through a homogeneous but absorbing and dispersive medium

Similarly, Eq. (7) can be rewritten as

$$\nabla^2\tilde{p}(\mathbf{r}) + (k_f^2 + i\epsilon)\tilde{p}(\mathbf{r}) = -S(\mathbf{r}) - \Big\{ - i\tau\omega(-\nabla^2)^{\nu/2} + \eta(-\nabla^2)^{(\nu+1)/2} - i\epsilon\Big\}\tilde{p}(\mathbf{r}). \tag{26}$$

The potential term can readily be recognized and for such a potential, the TBS procedure offers

$$\tilde{p}^{l+1}(\mathbf{r}) = \mathcal{F}^{-1}\Big[\tilde{g}(\mathbf{K})\Big[\{-i\tau\omega k^{\nu} + \eta k^{\nu+1} - i\epsilon\} \times \mathcal{F}\big[\tilde{p}^l(\mathbf{r})\big] + \mathcal{F}[S(\mathbf{r})]\Big]\Big]. \tag{27}$$

In this derivation, we have applied $\mathcal{F}[(-\nabla^2)^{\nu/2}\tilde{p}^l(\mathbf{r})] = k^{\nu}\mathcal{F}[\tilde{p}^l(\mathbf{r})]$. Note that fractional derivative operators along with their coefficients introduce frequency-dependent phase shift and amplitude decay, thereby producing power-law attenuation consistent with experimental measurement on biological media. The above expression has been computed to determine the steady state acoustic field generated by a linear array of point emitters when the medium is absorbing and dispersive.

3. Wave propagation through an inhomogeneous medium

Equation (10), after adding $i\epsilon\tilde{p}$ to both sides, transforms into

$$\nabla^2\tilde{p}(\mathbf{r}) + (k_f^2 + i\epsilon)\tilde{p}(\mathbf{r}) = -\mathcal{S}(\mathbf{r}) - (k_s^2 - k_f^2 - i\epsilon)\tilde{p}(\mathbf{r}). \tag{28}$$

Accordingly, one obtains

$$\tilde{p}^{l+1}(\mathbf{r}) = \begin{cases} \mathcal{F}^{-1}\Big[\tilde{g}(\mathbf{K})\mathcal{F}\Big[(k_s^2 - k_f^2 - i\epsilon)\tilde{p}^l(\mathbf{r}) + S(\mathbf{r})\Big]\Big], \\ \mathcal{F}^{-1}\big[\tilde{g}(\mathbf{K})\mathcal{F}\big[-i\epsilon\tilde{p}^l(\mathbf{r}) + S(\mathbf{r})\big]\big], \end{cases} \tag{29}$$

for inside and outside of the scatterer, respectively. Equation (29) is solved herein to evaluate the pressure field provided by an array of tiny sources in the presence of a scatterer. It may be mentioned here that Nobert Bojarski also utilized an analogous approach to study acoustic and electromagnetic scattering problems (Bojarski, 1982). In this study, the scattered field was obtained by solving a set of linear equations in the k-space (spatial Fourier transform space). The same method was further extended for calculating the time domain field.

4. Wave propagation through a nonlinear medium

Sub-equations of Eq. (12) are solved sequentially (one after another in a chain). For instance, the field for the 2nd harmonic depends on that of the 1st; similarly, the 3rd depends only on the 1st and 2nd, etc. Once the fields for the higher harmonics are known, then again, the sub-equations of Eq. (12) may be solved incorporating both the sum and difference terms. As a result of that, computational time would increase. In order to limit the computational time as well as to obtain reasonably accurate estimates of pressure fields, the sum terms can be retained and difference terms can be neglected. Accordingly, the source and potential terms, as per Eq. (14), can be distinguished without any difficulty for each equation. The corresponding solutions under the TBS framework take the forms

$$\mathcal{A}_1^{l+1}(\mathbf{r}) = \mathcal{F}^{-1}\Big[\tilde{g_1}(\mathbf{K})\mathcal{F}\Big[-i\epsilon_1\mathcal{A}_1^l + S\Big]\Big], \tag{30a}$$

$$\mathcal{A}_2^{l+1}(\mathbf{r}) = \mathcal{F}^{-1}\Big[\tilde{g_2}(\mathbf{K})\mathcal{F}\Big[-i\epsilon_2\mathcal{A}_2^l - \xi(2\omega)^2\frac{1}{2}\mathcal{A}_1\mathcal{A}_1\Big]\Big], \tag{30b}$$

$$\mathcal{A}_3^{l+1}(\mathbf{r}) = \mathcal{F}^{-1}\Big[\tilde{g_3}(\mathbf{K})\mathcal{F}\Big[-i\epsilon_3\mathcal{A}_3^l - \xi(3\omega)^2\mathcal{A}_1\mathcal{A}_2\Big]\Big], \tag{30c}$$

$$\mathcal{A}_4^{l+1}(\mathbf{r}) = \mathcal{F}^{-1}\Big[\tilde{g_4}(\mathbf{K})\mathcal{F}\Big[- i\epsilon_4\mathcal{A}_4^l - \xi(4\omega)^2 \times \Big[\frac{1}{2}\mathcal{A}_2\mathcal{A}_2 + \mathcal{A}_1\mathcal{A}_3\Big]\Big]\Big], \tag{30d}$$

$$\mathcal{A}_5^{l+1}(\mathbf{r}) = \mathcal{F}^{-1}\Big[\tilde{g_5}(\mathbf{K})\mathcal{F}\Big[- i\epsilon_5\mathcal{A}_5^l - \xi(5\omega)^2[\mathcal{A}_2\mathcal{A}_3 + \mathcal{A}_1\mathcal{A}_4]\Big]\Big], \tag{30e}$$

where $\quad \tilde{g}_n(\mathbf{K}) = \dfrac{1}{(|\mathbf{K}|^2 - n^2k_f^2 - i\epsilon_n)}.$

The series of equations furnished above have been numerically evaluated to estimate the pressure fields produced by the fundamental and higher harmonics for a nonlinear medium. Here, ϵ_n $(n = 1, 2, \ldots)$ denotes a harmonic-dependent constant. These constants are chosen individually for each harmonic to ensure numerical stability and convergence of the Born-series formulation.

III. NUMERICAL PROCEDURES

A. Numerical parameters

An representative diagram of an algorithm realizing the TBS procedure for linear media is presented as Algorithm 1. The computational domain consisted of 4096×4096 pixels with sides $dx = dy = 20$ μm. Therefore, different matrix operations like initialization, addition, and multiplication were performed on 4096×4096 matrices. Here, the matrices mean S, V, $g(\mathbf{K})$, $\tilde{p}_{in}$, $\tilde{p}_{fn}$, and *ABL2DM*; *ABL2DM* represents a two-dimensional (2D) mask consisting of an absorbing layer (ABL) at each boundary, as shown in Fig. 1. The speed of sound and density of the medium were fixed to, $v_f = 1500$ m/s and $\rho_f = 1000$ kg/m^3. A linear array of point sources was placed at a distance $x_{el} = 675dx$ from the left edge, as shown

ALGORITHM 1: Acoustic field calculation using the TBS algorithm for linear and nonlinear media.

Input : Initialize system parameters Prepare computational domain: N_{cn}, $\mathcal{K}_{cn}$, dx, *ABL2DM* Convergence limit: *ThError* Transducer properties: f, *Nel*, x_{el}, yel Medium properties: $u_f, \alpha, \tau, \eta, \nu, B/A$ Scatterer properties: v_s, a

Output : PA field $\tilde{p}f_n$

1 **for** $i \leftarrow 1$ **to** 5 **do**
   `// Restrict` $i=1$ `for linear media`
2 $f \leftarrow i \times 55 \times v_f/(N_{cn} \times dx)$
3 $\omega \leftarrow 2\pi f$
4 $k_s \leftarrow \omega/v_s$
5 $k_f \leftarrow \omega/v_f$
6 $\in \ \leftarrow 0.8k_f^2$
7 **for** $j \leftarrow 0$ **to** $N_{cn}-1$ **do**
8 **for** $m \leftarrow 0$ **to** $N_{cn}-1$ **do**
9 $index \leftarrow j \times N_{cn} + m$
10 $\mathcal{K}_x \leftarrow 2\pi(m-\mathcal{K}_{cn})/(N_{cn}dx)$
11 $\mathcal{K}_y \leftarrow 2\pi(j-\mathcal{K}_{cn})/(N_{cn}dx)$
12 $Kmod[index] \leftarrow \sqrt{\mathcal{K}_x^2+\mathcal{K}_y^2}$
13 $g\mathcal{K}[index] \leftarrow \left(\frac{\mathcal{K}_x^2+\mathcal{K}_y^2-k_f^2}{(\mathcal{K}_x^2+\mathcal{K}_y^2-k_f^2)^2+\in^2}, \frac{\in}{(\mathcal{K}_x^2+\mathcal{K}_y^2-k_f^2)^2+\in^2}\right)$
14 $S[index] \leftarrow (0.0, 0.0)$
15 **if** $(i == 1)$ **then**
16 **if** $(j == x_{el} \&\& m == y_{el})$ **then**
17 $S[index] \leftarrow (0.0, -1\times10^6)$
18 end
19 else
20 $S[index] \leftarrow \xi(\omega)^2 \times (\text{sum terms})$ `// From Eq. (30)`
21 end
   `// Case I: Homogeneous medium`
22 $V[index] \leftarrow (0.0, -\epsilon)$
   `// Case II: Absorbing/dispersive medium`
23 $VV[index] \leftarrow (\eta kmod^{v+1}, -\tau\omega kkmod^{v} - \epsilon)$
   `// Case III: Heterogeneous medium`
24 $dist \leftarrow \sqrt{(m-\mathcal{K}_{cn})^2+(j-\mathcal{K}_{cn})^2}dx$
25 **if** $dist \leq a$ **then**
26 $V[index] \leftarrow (k_s^2 - k_f^2, -\epsilon)$
27 **end**
28 **else**
29 $V[index] \leftarrow (0.0, -\epsilon)$
30 **end**
   // Case IV: Nonlinear medium
31 $V[index] \leftarrow (0.0, -\epsilon)$
32 **end**
33 **end**
34 $g\mathcal{K} \leftarrow \text{fftShift}(g\mathcal{K})$
35 $kmod \leftarrow \text{fftShift}(g\mathcal{K})$
36 $VV \leftarrow \text{fftShift}(VV)$
37 $\tilde{p}_{in} \leftarrow \text{ifft}(g\mathcal{K} \times \text{fft}(S))$
38 **for** $iter \leftarrow 1$ **to** 2000 **do**
   `// Case I, III, IV:`
39 $\tilde{p}_{fn} \leftarrow \text{ifft}(g\mathcal{K} \times \text{fft}(V \times \tilde{p}_{in} + S)) \times ABL2DM$
   `// Case II:`
40 $\tilde{p}_{fn} \leftarrow \text{ifft}(g\mathcal{K} \times (VV \times \tilde{p}_{in} + \text{fft}(S))) \times ABL2DM$
41 $error \leftarrow \frac{\|\tilde{p}_{fn}[N_{cn}/2] - \tilde{p}_{in}[N_{cn}/2,:]\|}{\|\tilde{p}_{fn}[N_{cn}/2,:]\|}$
42 **if** $error < ThError$ **then**
43 $saturationTBS \leftarrow iter$
44 **break**
45 **end**
46 $\tilde{p}_{in} \leftarrow \tilde{p}_{fn}$
47 **end**
48 **end**

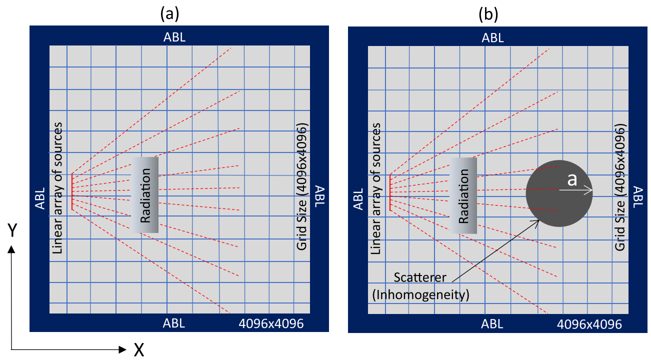

FIG. 1. Schematic diagram of the computational domain (size 4096×4096, resolution $dx = dy = 20\ \mu$m). (a) The propagating medium is homogeneous but either lossless or lossy (absorbing/absorbing-dispersive) or nonlinear. (b) The propagating medium encloses a scattering region. ABL refers to absorbing layer.

in Fig. 1, with a strength of $|S| = 1\,000\,000$ Pa/m^2. (The amplitude of the pressure field depends upon the magnitude of S.)

The source points were symmetrically positioned with respect to the row number $y_{el} = 2049dx$. A total number of $N_{el} = 501$ grid points acted as the acoustic sources replicating a line source of width $500dx$. In other words, this could be written as

$$\begin{aligned} &\text{Step 1:}\ \ S(m,n) = 0 - i0, &&\text{with} \quad \text{m, n} \in [1..4096], \\ &\text{Step 2:}\ \ S(m,675) = 0 - i10^6, &&\text{with} \quad \text{m} \in [1799..2299]. \end{aligned} \tag{31}$$

The block from lines 14 to 21 of Algorithm 1 realized the above steps. Furthermore, the same $S(\mathbf{r})$ was used in all subsequent cases. Algorithm 1 also demonstrates how to build the $g(\mathbf{K})$ matrix (see line 13); V matrices for different cases are described from lines 22 to 31. The initial field was estimated by implementing Eq. (23). After that, for the homogeneous and lossless medium, Eq. (25) was calculated iteratively to obtain the spatial distribution of pressure field for $f = 1\,007\,080$ Hz using $\epsilon = 0.8k_f^2$ (Kaushik *et al.*, 2020; Osnabrugge *et al.*, 2016; Saha, 2020, 2021; Mandal *et al.*, 2025); this particular choice was made based on the literature because it provided a good balance between computational accuracy and convergence speed (Osnabrugge *et al.*, 2016). The chosen frequency $f = 1007080$ Hz is the 55th multiple of the fundamental frequency supported by this grid system ($v_f/(4096dx)$). Note that after each iteration, the pressure field $\tilde{p}^{l+1}$ was multiplied by the *ABL2DM* matrix. The entries at the boundary grid points (i.e., inside the two vertical and two horizontal strips, as demonstrated in Fig. 1) of this matrix were defined via a sigmoid function as given below (Mandal *et al.*, 2025),

$$f_{\text{ABL}}(q) = \frac{1}{1+\exp(-\zeta(q-0.5\mu))} \ \text{within the ABL}, \tag{32}$$

where $q > 0$. Here, q is the distance of a grid point within the boundary layer from the nearest grid point lying at the outermost layer of the inner region (white region of Fig. 1); ζ was chosen to be $\zeta = 21.48$ Np/cm for all frequencies.

However, unity was assigned to the remaining grid points of the *ABL2DM* matrix. This sigmoid function essentially built the absorbing layer. The width of the ABL was $\mu = 450dx$. It was designed with a nonlinear absorption property. This layer ensured that an outgoing wave was absorbed effectively and exiting a boundary did not reemerge from the opposite side, preventing wave wrapping associated with the Fourier transformation operation (Treeby and Cox, 2010b). It is the artifact of the discrete Fourier transform, and aliasing in the spatial domain and the boundary layer considered in this study (attenuation is modeled by the sigmoid function) can effectively suppress the artifact. The field was supposed to converge if the error was $< 10^{-5}$. The error was obtained as

$$\text{Total error} = \frac{\sum_{m=1}^{4096} |\tilde{p}_{l+1}(2049, m) - \tilde{p}_l(2049, m)|}{\sum_{m=1}^{4096} |\tilde{p}_l(2049, m)|}. \quad (33)$$

A maximum number of 2000 iterations was set in all simulations. An algorithm applying the TBS scheme in the context of photoacoustics can be found in Kaushik *et al.* (2020). MATLAB implementations of the Born series methods are available in Saha (2025a).

Similarly, Eq. (27) was implemented to yield the field distribution for the same transducer in an absorbing and dispersive medium having $\alpha_0 = 5.5 \times 10^{-10}\,\text{Np(rad/s)}^{\nu}\ \text{m}^{-1}$ and $\nu = 1.5$ (Treeby and Cox, 2010b); this numerical value of α_0 also corresponds to $\alpha_0 = 0.75$ dB MHz$^{-\nu}$ cm^{-1}. Accordingly, τ and η could be computed to be $\tau = -2\alpha_0 v_f^{\nu-1}$ and $\eta = 2\alpha_0 v_f^{\nu} \tan(\pi\nu/2)$. The initial field was determined as that of the previous case. For the inhomogeneous case, Eq. (29) was numerically realized by repeating the same procedure. The speed of sound inside the scatterer was varied from $v_s = 1350$ to $1800\,\text{m/s}$, with a step of 150 m/s. The radius of the inhomogeneity was taken as $a = 50dx = 1$ mm with size parameter $k_f a = 4.22$. It is positioned at $x = 40.2$ mm away from the center of the acoustic line source. It might be noted that no smoothing operation was made to remove the sharp edges of the scatterer.

Finally, pressure fields for a nonlinear medium for the same transducer were assessed for the fundamental frequency as well as up to the 5th harmonic. The wave equations are given in Eqs. (12), and the corresponding TBS solutions are provided in Eqs. (30), while keeping the sum terms only. The TBS algorithm implemented for this purpose is detailed in Algorithm 1. At first, the pressure field for the fundamental frequency was evaluated for $|S| = 10^8\,\text{Pa/m}^2$. After that, fields were calculated for higher harmonics one by one. The numerical values of $\epsilon_n = 0.8n^2k_f^2$ and

$$\tilde{g}_n(\mathbf{K}) = \frac{1}{(|\mathbf{K}|^2 - n^2k_f^2 - i\epsilon_n)}$$

were appropriately calculated for each harmonic (Kaushik *et al.*, 2020; Osnabrugge *et al.*, 2016; Saha, 2020, 2021; Mandal *et al.*, 2025); B/A was assigned to be 5 (Beyer, 2008). In biomedical US harmonic imaging, conventionally, echoes facilitated by the fundamental and 2nd harmonic are utilized to generate two separate images (Anvari *et al.*, 2015; Gan, 2021). It is seen that the 2nd harmonic image provides more details than the fundamental. The intensity of the 2nd harmonic echo is 10–20 dB lower than that of the fundamental frequency. Other higher harmonic components are even weaker than this level and hence difficult to use for imaging purposes. That is why in this work, for demonstration purposes, we considered pressure fields for first five harmonics only.

B. GPU acceleration strategy

The computational demands of the TBS algorithm primarily arose from large-scale matrix operations, making it highly suitable for GPU acceleration. We implemented a parallel computing approach using Nvidia's CUDA architecture to optimize the performance (Sanders and Kandrot, 2011). Note that CUDA is an application programming interface (API), and the implementation leverages CUDA's general-purpose computing capabilities (GPGPU). The CUDA framework allows direct access to GPU hardware resources through specialized compute kernels. To minimize data transfer overhead, all matrices were allocated directly in GPU device memory. Therefore, host-to-device copy operations were eliminated for core computational matrices. Furthermore, coalesced memory access was enabled.

The pressure field distributions at the steady state for various media were calculated by running the TBS codes written in the CUDA C programming language. Required matrices were initialized as arrays carrying double precision real numbers, and also the operations were performed using the double precision arithmetic. The iterations associated with the for loops from lines 7 to 32 in Algorithm 1 can be carried out independently. These loops were processed in parallel using a GPU kernel (each GPU thread independently calculated lines from 9 to 31 for a combination of j and m indices), and therefore, various matrices (e.g., S, V, VV, $g(\mathbf{K})$) could be constructed very rapidly. Matrix operations like addition, subtraction, and multiplication were implemented as separate optimized kernels (see lines 39–46 of Algorithm 1). As mentioned earlier, all these matrix operations happened to be element-wise (independent of each other), and thus, massive parallelization could be accomplished utilizing a large number of GPU threads. As a result of that, tremendous acceleration could be achieved. The number of kernels was restricted to as minimum as possible since launching a CUDA kernel involves some overhead for setting up the execution environment. The forward and backward fast Fourier transforms (FFTs) were calculated utilizing a cuFFT library function, namely cufftExecZ2Z. All simulations were performed on a workstation with GPU computation facility. The specifications of the machine are included in Table II. GPU codes can be found in Saha (2025b).

C. Central processing unit (CPU) parallelization strategy

The TBS algorithm was also implemented in C for CPU execution in the same machine (see Table II) with double

https://doi.org/10.1121/10.0042817

TABLE II. Description of the computational resources used for numerical calculations.

Feature	Description
CPU model	AMD Ryzen Threadripper PRO 5965WX 24-Cores @4569.0000 MHz[a]
No. of CPU cores	24
No. of threads per core	2
No. of cores per socket	24
Architecture	x86_64, 64-bit
Operating system (OS)	UBUNTU 24.04.2 LTS
GPU model	Nvidia GeForce RTX 4060 @2.475 GHz[b]
No. of CUDA cores	3072
GPU driver version	570.124.06
No. of GPUs	1
GPU RAM	8 GB
CPU RAM	256 GB
CUDA toolkit version	12.8
MATLAB version	2023b

[a]AMD, Santa Clara, CA.
[b]Nvidia, Santa Clara, CA.

precision computations. The purpose of this study was to investigate how fast the GPU codes could be executed compared to the CPU counterparts. We parallelized computationally intensive loops using OpenMP (Open Multi-Processing), an industry-standard API for shared-memory parallelism, and it can leverage modern multi-core CPU architectures for faster execution of codes too (Eijkhout, 2022). This API is capable to realize dynamic scheduling to balance workload distribution, minimizing thread idle time and also to prevent false sharing and cache contention. Outer loop iterations were parallelized. This approach significantly accelerated matrix operations, particularly for nested loops where independent iterations could be processed concurrently. The FFTW library was utilized for optimized calculation for forward and inverse FFTs. CPU codes can be accessed from Saha (2025b).

D. Computations using the *k*-space pseudospectral technique

The numerically evaluated pressure fields facilitated by the TBS approach were compared with that of a standard, MATLAB-based and freely available software (K-WAVE toolbox). This is a widely accepted numerical tool for solving wave propagation problems, particularly in heterogeneous and nonlinear media. It provides an accurate time-domain solution to the full wave equation. It might be worth mentioning that K-WAVE has been extensively validated both against other numerical models (linear and nonlinear) and against analytical solutions (linear and nonlinear) and experimental data as well (Treeby *et al.*, 2012; Martin *et al.*, 2020; Aubry *et al.*, 2022). Comparison with K-WAVE validates the accuracy and effectiveness of the TBS. However, other numerical methods could also be utilized for the same. The theoretical background of the K-WAVE module and its implementation details can be found in the literature (Treeby and Cox, 2010a,b). For the sake of completeness, this procedure is briefly discussed here. In this approach, instead of second order partial differential equation, coupled first order partial differential equations are numerically solved. The most general forms of the coupled partial differential equations incorporating all medium dependent scenarios are (Treeby and Cox, 2010a)

$$\frac{\partial \mathbf{u}}{\partial t} = -\frac{1}{\rho_f}\nabla\tilde{p} + S_F, \tag{34a}$$

$$\frac{\partial \rho}{\partial t} = -(2\rho + \rho_f)\nabla\cdot\mathbf{u} - \mathbf{u}\cdot\nabla\rho_f + S_M, \tag{34b}$$

$$\tilde{p} = v_f^2\left(\rho + \mathbf{d}\cdot\nabla + \frac{B}{2A}\frac{\rho^2}{\rho_f} - L_{frac}\right). \tag{34c}$$

Here, the fractional Laplacian is defined as

$$L_{frac} = \tau\frac{\partial}{\partial t}(-\nabla^2)^{(v/2)-1} + \eta(-\nabla^2)^{(v+1)/2-1}.$$

$\mathbf{u}$ is the acoustic particle velocity, and ρ is the density. Furthermore, S_F is a force source term and represents the input of body forces per unit mass and S_M is a mass source term and represents the time rate of the input of mass per unit volume. Note that in the preceding wave equations, the mass source term has been considered (ignoring the force source term). Equations (34) demonstrate the momentum conservation, mass conservation, and pressure density relation, respectively. The above differential equations are efficiently calculated in the K-WAVE module, using a pseudospectral model that computes spatial gradients using Fourier collocation and the time-stepping uses a dispersion-corrected finite difference approach. Additionally, staggering is used in space and time for reasons of stability and to improve accuracy for heterogeneous simulations.

The size of the computational domain and the grid spacing were the same as those of the previous simulations (4096×4096, $dx = dy = 0.02 \times 10^{-3}$ m). The thickness of the perfectly matched layer was chosen to be $30dx$. A linear array of acoustic sources was placed at the 40th grid-location from the outermost left boundary with strength source.p = 1 000 000 Pa (see Fig. 1). The source points occupied the exact same locations along the y-direction as that of the TBS method, as shown in Fig. 1. The medium properties were set case by case as described above. The Courant–Friedrichs–Lewy number was fixed to 0.3 for the K-WAVE simulations to ensure numerical stability. The time step was automatically fixed by the K-WAVE toolbox. Then the GPU version of the K-WAVE function, namely, kspaceFirstOrder2DG was executed in the same workstation with double precision mode turned on (Treeby and Cox, 2010a). The steady state pressure data for three periods (750 data points, which was arbitrarily chosen) for each grid location were acquired, and this sequence was repeated 23 times, providing a long one-dimensional (1D) array. Such time series data for each grid point were then Fourier transformed (by performing 16 384-point FFT), and subsequently, numerical values of amplitude and phase at

$f = 1\,007\,080$ Hz as well as the same for harmonics (for nonlinear medium) were stored (from the Fourier transformed data). This procedure was reiterated for all grid crossings. The next step was to generate a 2D map of amplitude and phase for comparison with the TBS counterparts. The above workflow was exactly followed for the nonlinear case as well, but in this case, amplitude and phase at multiple frequencies, i.e., $f = 1\,007\,080$, $2\,014\,160$, $3\,021\,240$, $4\,028\,320$, and $5\,035\,400$ Hz, were saved from the spectral data.

IV. NUMERICAL RESULTS

Figure 2 presents the simulated fields using the TBS and K-WAVE methods for a linear array of point sources. The point sources are sinusoidally oscillating with a frequency of $f = 1\,007\,080$ Hz. The propagating medium is homogeneous and lossless. Perfect agreement can be seen between the two approaches. As expected, field near to the line source exhibits fluctuations owing to the diffraction effect (near field). In the far field, the mainlobe dominates and it varies smoothly. In other words, most of the energy of the beam is packaged within a small angular region. The existence of the sidelobes can also be noticed from Figs. 2(a) and 2(c). The phase part changes between $-\pi$ and π. The on and off axis profiles look identical for the two approaches. The actual pressure field (in pascals) produced by the TBS method is included in Fig. S1(a) in the supplementary material when the source strength is $|S| = 1\,000\,000$ Pa/m^2. The same plot for the K-WAVE method is presented in Fig. S1(b) for source.p $= 1\,000\,000$ Pa. In order to reproduce the K-WAVE result, a factor of $\omega/v_f dx$ has to be multiplied with the TBS result in two dimensions. For three dimensions, the factor would become $2\omega/3v_f dx$.

Similar figures for the absorbing and dispersive medium are shown in Fig. 3. The phase maps are given in Fig. S2. As in the previous case, both procedures demonstrate an exact match. It may be noted that pressure amplitude in the far field rapidly falls off for the mainlobe due to the absorption property of the medium. Compared to the lossless case, the ultrasonic beam penetrates less in the lossy medium. The same plots for the absorbing medium are included in Fig. S3 in the supplementary material.

The spatial distributions of normalized pressure amplitude and line plots are shown in Fig. 4 when the medium contains a scattering region. Figure S4 in the supplementary material presents the corresponding phase maps. The scatterer has a diameter of $a = 1$ mm. It is placed on the axis of the line source and $x = 40.2$ mm away from the acoustic source. The speed of sound mismatch is about 10% with respect to that of the ambient medium ($v_s = 1650$ m/s, $v_f = 1500$ m/s). TBS and K-WAVE results appear identical. The field pattern up to the source location is analogous to that of the homogeneous and lossless medium [compare Figs. 4(a) and 2(a)]. After the inhomogeneity, the most of the beam energy splits into two angular directions (symmetrical with respect to the axis). Additional results for

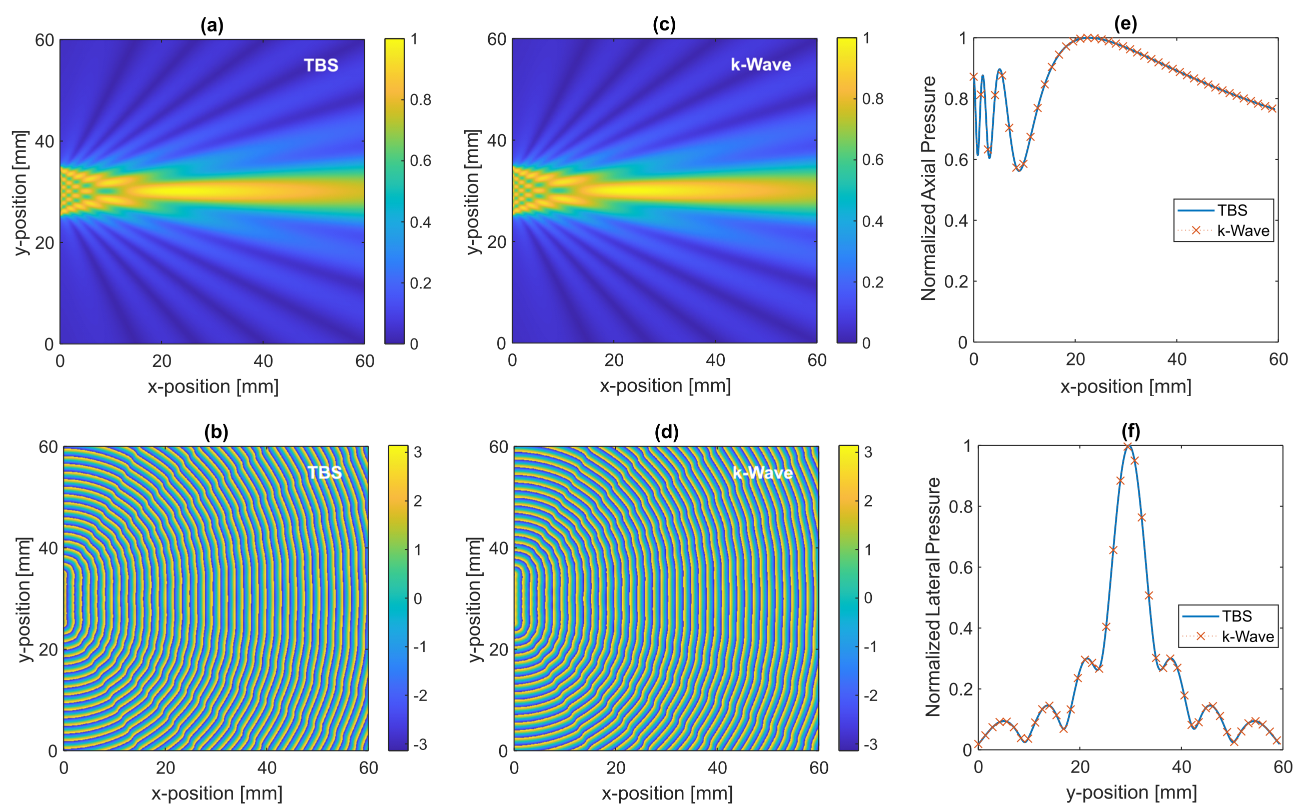

FIG. 2. (a) and (b) Steady state normalized field pattern and spatial distribution of phase for a linear array source with 501 point elements calculated using the TBS method for the homogeneous and lossless medium. (c) and (d) Same as (a) and (b) but for the K-WAVE technique, respectively. (e) Steady state acoustic normalized pressure amplitude along the axis of the transducer. (f) Same as (e) but for the lateral direction, at a distance $x \approx 41$ mm from the transducer.

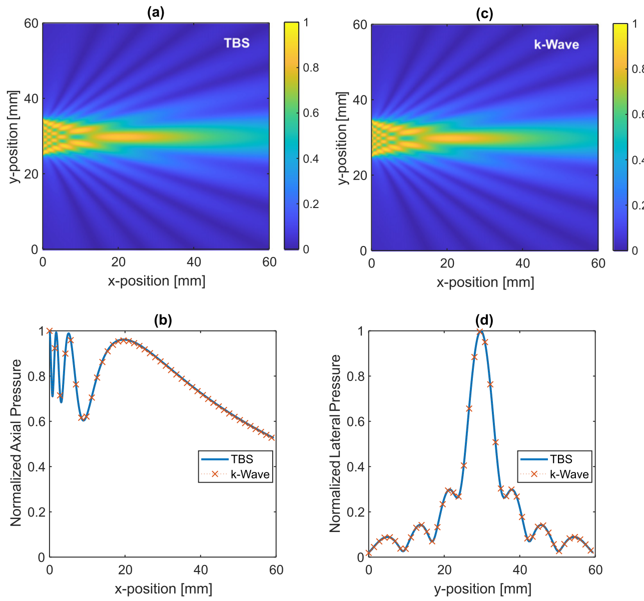

FIG. 3. Same as Fig. 4 but for the absorbing and dispersive medium.

$v_s = 1350$ and $1800\,\text{m/s}$ are shown in Figs. S5 and S6, respectively, in the supplementary material.

The simulated field patterns for the nonlinear medium are displayed in Fig. 5 in detail. The field distributions created by the TBS methods are shown in the top row sequentially from 2nd to 5th harmonics, i.e., $f = 2\,014\,160$, $3\,021\,240$, $4\,028\,320$, and $5\,035\,400$ Hz [Figs. 5(a)–6(d)]. The same results produced by the K-WAVE are portrayed in the second row. The TBS result duplicates K-WAVE estimations. It is evident from this figure that the region with maximum pressure amplitude shifts towards the right (i.e., away from the source) as the frequency grows. The axial and lateral line profiles are drawn and depicted in the third and fourth rows, respectively. Up to 3rd harmonics profiles are almost overlapping. However, for the 4th and 5th harmonics, K-WAVE results deviate from that of the TBS technique. Reflections from the boundary occur for these harmonics [see Figs. 5(g) and 5(h)]. In general, the simulated results of both the methods agree well, which indirectly confirms that the sum terms provide reasonably good estimates for the harmonic fields.

The memory requirement for the TBS formulation was about 2.7 GB (mostly contributed by seven complex and three real double precision arrays) for the linear media. The same for the K-WAVE methodology was nearly 750 MB. The TBS technique does not take long iterations to converge, as can be seen from Table III. The number of iterations (column 2) has been counted to be $\sim$135 for the fundamental frequency. The execution time for each case is also given in the same table (column 3), and it depends upon the number of matrix operations involved for calculating the field. For instance, computation time for the absorbing and dispersive medium is higher than that for the lossless medium since Eq. (27) is more complex than Eq. (25). The average execution time is estimated to be around 7.5 s for $f = 1\,007\,080$ Hz, whereas the same quantity for the K-WAVE simulation is nearly 580 s. Therefore, nearly $77\times$ speed up can be achieved by the TBS method. It may be pointed out that a parallel CPU code took 21 s for the homogeneous case in the same computer specified in Table II (speed up $\sim 4\times$). All details for the other CPU codes can be found in the same table (Table III). It is also visible from Table III that number of iterations *vis-á-vis* computation time increases progressively as the frequency increases for the nonlinear medium [i.e., sub-equations of Eq. (30)]. Note that convergence reaches quickly if the initial field (0-th iteration) is strong. Nevertheless, higher iteration is required if the initial field is weak (see for higher harmonics).

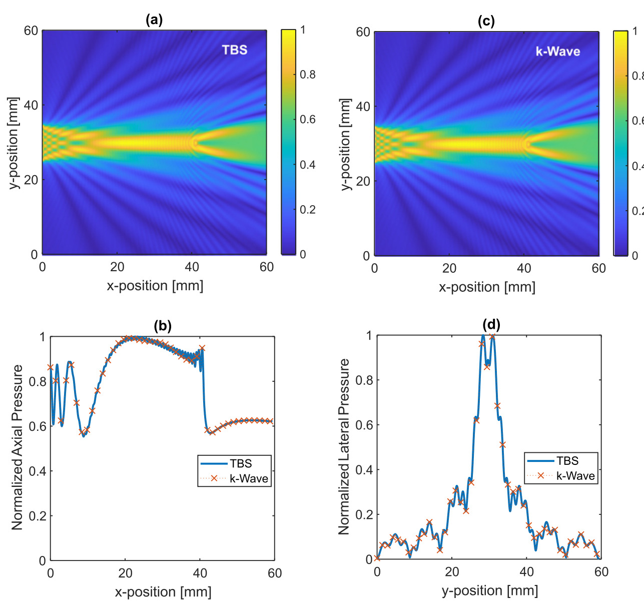

FIG. 4. (a) and (b) Steady state spatial distribution of normalized pressure amplitude for the same linear array of sources and calculated using the TBS method for an inhomogeneous medium ($v_f = 1500$ m/s, $v_s = 1650$ m/s). The scatterer (of radius $a = 1$ mm) and the transducer are separated by a distance of $x = 40.2$ mm. (c) and (d) Simulated results for the K-WAVE procedure as of (a) and (b), respectively. (e) and (f) Plots of on and off axis profiles for the normalized pressure amplitude (off axis distance from the line source is $x \approx 41$ mm).

V. DISCUSSION

In this study, we have provided detailed derivations of the TBS framework for transducer field calculations for a series of realistic media, namely, homogeneous and lossless, absorbing and dispersive, and inhomogeneous and nonlinear. Accordingly, the source and potential terms have been identified for different cases by examining the conventional wave equations. After that, the Green's function method has been applied to calculate the steady state solutions. The solutions are presented in terms of infinite series sums. In each case, field and phase characteristics for a line source are investigated. To compare the TBS results, K-WAVE simulations have also been conducted. Perfect match between the field maps facilitated by the two methods can be seen. Phase maps also exhibit excellent match. The mean phase error between the TBS and K-WAVE outcomes was found to be 1.5 mrads. The results suggest that the frequency domain and time domain approaches provide consistent results, with only minimal

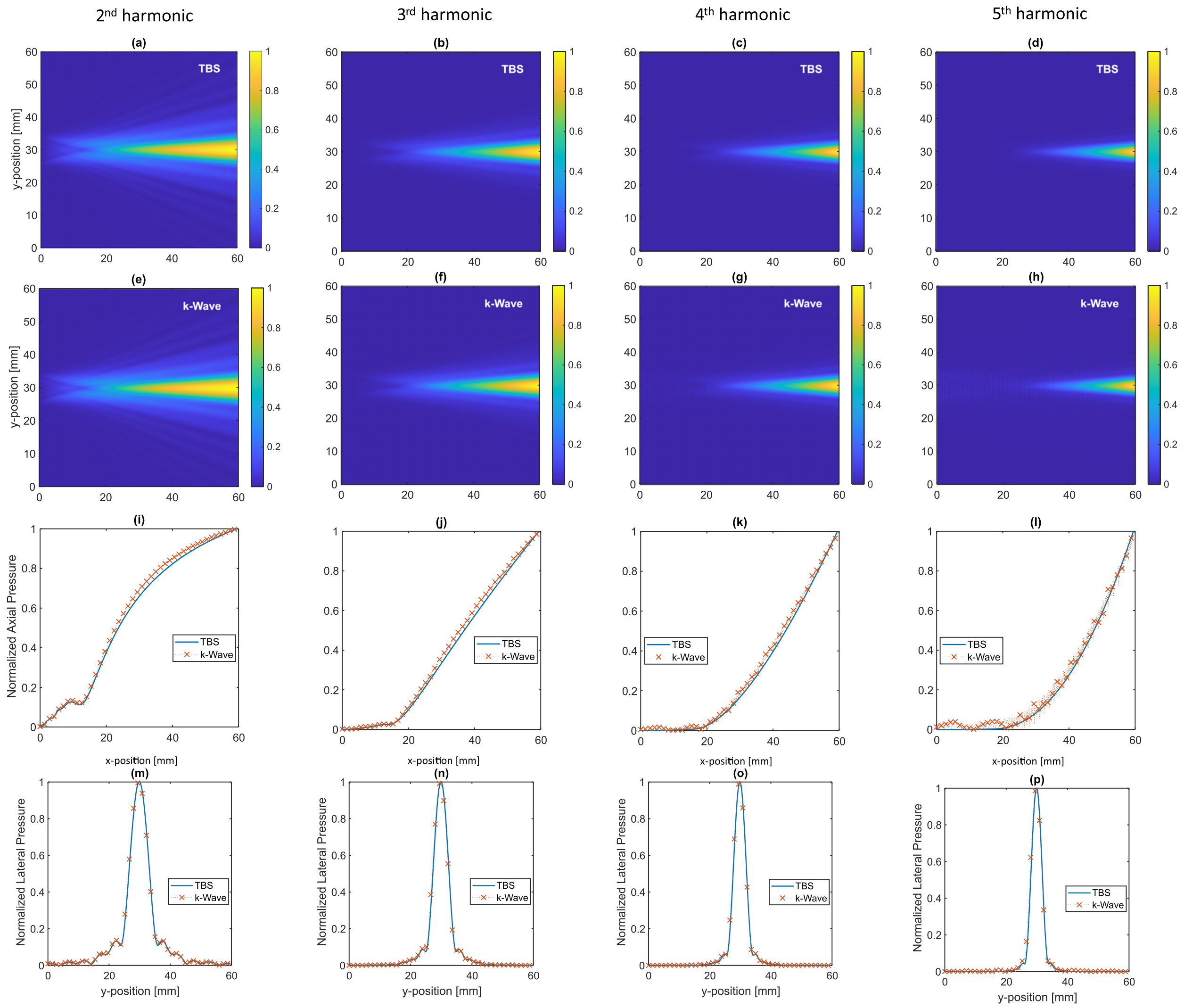

FIG. 5. (a)–(d) Steady state normalized pressure field estimated by the TBS algorithm for 1st, 2nd, 3rd, and 4th harmonics. (e)–(h) Analogous plots but simulated via the K-WAVE package. (i)–(l) On axis variation of the steady state normalized pressure amplitude for the TBS and K-WAVE schemes. (m)–(p) Demonstration of the off axis normalized pressure amplitude by the same methods at $x \approx 58$ mm from the transducer.

discrepancies that may arise due to numerical approximations, interpolation artifacts, or differences in boundary conditions.

The numerical value of ϵ was chosen to be $\epsilon = 0.8k_f^2$ in the present study (Kaushik *et al.*, 2020; Osnabrugge *et al.*, 2016; Saha, 2020, 2021; Mandal *et al.*, 2025). Note that the medium becomes more attenuating, and thus, the disturbance spreads slowly as the strength of ϵ increases. As a result of that, the TBS technique takes more iterations to converge. In other words, the number of iterations can be reduced by decreasing ϵ (Saha, 2020). Furthermore, the TBS method does not impose any restriction on the choice of magnitude of ϵ; however, $\epsilon \geq \max(k_s^2 - k_f^2)$ is required for the convergence of the CBS method for a heterogeneous medium (Osnabrugge *et al.*, 2016). As mentioned earlier, the CBS method works well even when a large and strong scattering region or regions are present within the computational domain (Mandal *et al.*, 2025). Attempts will be made in future to implement the CBS algorithm for transducer pressure field calculation in realistic media. The method or its analogues have been developed further in the geophysics community, but including renormalization group theory and homotopy continuation approaches (Jakobsen *et al.*, 2020a; Jakobson *et al*, 2020b).

Table IV highlights the impact of various parameters on the convergence of the TBS method. At first, it is observed that the TBS method converges until 2 points per wavelength is taken. For the second medium, convergence can be achieved for $\nu \leq 1.7$ for the given α_0, beyond which it diverges. Further, $\tau > -4.3 \times 10^{-5}$ and $\eta > -6.4 \times 10^{-3}$ for convergence (see rows 4 and 5, respectively). It is worth mentioning here that, while here we have used the absorption model that is built into K-WAVE, for purposes of comparison, the nonlinear TBS approach is not restricted to a specific absorption model. In principle, any spatially varying absorption and dispersion, with any frequency dependence, could be incorporated into the potential. For the fourth medium, the TBS method produces faithful results over a large range of sound-speed mismatch: $v_s = 1100$ to 3750 m/s. We have seen that convergence of the TBS technique is independent of the magnitude of B/A. This is obvious because B/A or ξ controls the strength of S at higher

TABLE III. Iterations (Iter.) and execution times (T) for convergence under different media. Inhom., inhomogeneous; harm., harmonic; N/A, not applicable.

Medium	GPU		CPU		K-WAVE T (s)
	Iter.	T (s)	Iter.	T (s)	
Homogeneous	135	5	133	21	512
Absorbing	133	8	134	31	694
Absorbing-dispersive	132	11	131	32	520
Inhom., $v_s = 1350$ m/s	134	7	162	27	568
Inhom., $v_s = 1650$ m/s	134	7	155	25	566
Inhom., $v_s = 1800$ m/s	134	7	164	27	622
Nonlinear 1st harm.	135	5	133	21	511
Nonlinear 2nd harm.	228	9	225	34	N/A
Nonlinear 3rd harm.	306	12	301	45	N/A
Nonlinear 4th harm.	368	15	362	55	N/A
Nonlinear 5th harm.	416	16	409	61	N/A

harmonics, which may be arbitrary. (V is more critical than S for convergence of the TBS algorithm.)

It is important to note that boundary condition plays a crucial role for obtaining accurate results in numerical field calculations. For the TBS method, we applied a sigmoid function to dampen the outgoing wave. This function has been phenomenologically chosen and found to work exceedingly well for fundamental frequency as well as harmonics (see the first row of Fig. 5). The function at first very slowly decays from unity, and thus, the wave would not reflect back; on the other hand, it decays very slowly attaining zero, ensuring that the wave would not reemerge from the opposite boundary while leaving a boundary (minimizing wave wrapping). Wave wrapping is a serious issue that is associated with the extensive usage of the forward and inverse FFTs. The K-WAVE method uses a perfectly matched layer to attenuate the signal, where the normal component (with respect to the boundary surface) of the particle velocity is gradually reduced leaving the parallel component unaltered. It may be pointed out that in case of CBS technique, a potential was assigned to each boundary layer causing absorption of the outgoing wave. The same group has also developed a method, which builds a pretty thin absorbing layer (much thinner than that of the present work) (Osnabrugge *et al.*, 2021).

The pressured fields for various realistic tissue media have been generated in this study. For simplicity, each medium was considered one at a time. However, a realistic medium can simultaneously retain several properties. In order to examine the applicability of the TBS technique for such a medium, wave propagation through an inhomogeneous, absorbing and dispersive medium has been simulated. The computational scenario is illustrated in Fig. 6(a). The beam is steered approximately by 9° by gradually varying the phase from 0 to 2π between the extreme source points. Figure 6(b) plots the same beam for the absorbing and dispersive medium only. The resultant beams (propagating through the absorbing, dispersive medium and interacting with the scatterers) generated by the TBS and K-WAVE methods are displayed in Figs. 6(c) and 6(d), respectively. The difference map confirms that the TBS method can accurately reproduce the pressure field even for a complex medium (maximum error is $\approx 2.0\%$) [Fig. 6(e)].

TABLE IV. Convergence test for the TBS method. The units of the parameters are mentioned previously.

Parameter	Constant parameters	Range	Convergence
$v_f/(fdx)$		≥ 2	✓
ν	$\alpha_0 = 5.5 \times 10^{-10}$	≤ 1.7	✓
τ	$\nu = 1.5, \eta = -6.4 \times 10^{-5}$	-10^{-5} to 10^{-6}	✓
η	$\nu = 1.5, \tau = -4.3 \times 10^{-8}$	-10^{-3} to 10^{-3}	✓
v_s	$a = 1, v_f = 1500$	1100–3750	✓
B/A		Arbitrary	✓

The numerical study has been carried out for a 2D computational domain. Subsequently, the pressure field generated by a linear array of sources (line source) is computed for different realistic tissue properties. A practical diagnostic US array transducer is a 3D system (where small rectangular piezoelectric elements are glued on a backing layer in an ordered manner). We plan to implement the TBS/CBS method for field and signal calculations by realistic transducers (3D systems) in the near future. It may be noted that memory requirement will increase significantly for performing 3D simulations. For example, various matrices would occupy about 68 GB of memory for a computational domain of $1024 \times 1024 \times 1024$ grid points, assuming a single precision data type. Moreover, a smaller number of grid points per wavelength (e.g., 15 grid points instead of 75 points per wavelength as of the current implementation) and multiple GPUs may be deployed to tackle the memory issue. Additional validation with other theoretical models, numerical schemes, and experimental results (e.g., underwater measurement with a hydrophone and US probe to determine fields at harmonics) will be also be carried out subsequently. In particular, Burger's equation can be solved using the spectral method, which may be compared with the Born series result (Christopher and Parker, 1991).

VI. CONCLUSIONS

In conclusion, the TBS method is a standard and established technique to solve the inhomogeneous Helmholtz equation. Conventionally, it has been extensively used to solve such an equation arising in potential scattering problems (Sakurai, 1967; Bransden and Joachain, 2003). The TBS algorithm has been implemented in this work to yield a solution to the same equation occurring in the context of biomedical ultrasonics. Note that acoustic wave propagation, through a homogeneous and lossless tissue medium, can essentially be modeled by the homogeneous Helmholtz equation when the region of interest does not contain any acoustic source. Nevertheless, the equation becomes inhomogeneous for a lossy or a nonlinear tissue medium or when a tissue retains scatterers (due to small fluctuations in physical and chemical properties) even in the absence of an acoustic source. Acoustic field distributions were computed for a line source by the TBS method for various realistic media mentioned above; K-WAVE simulations were also conducted for

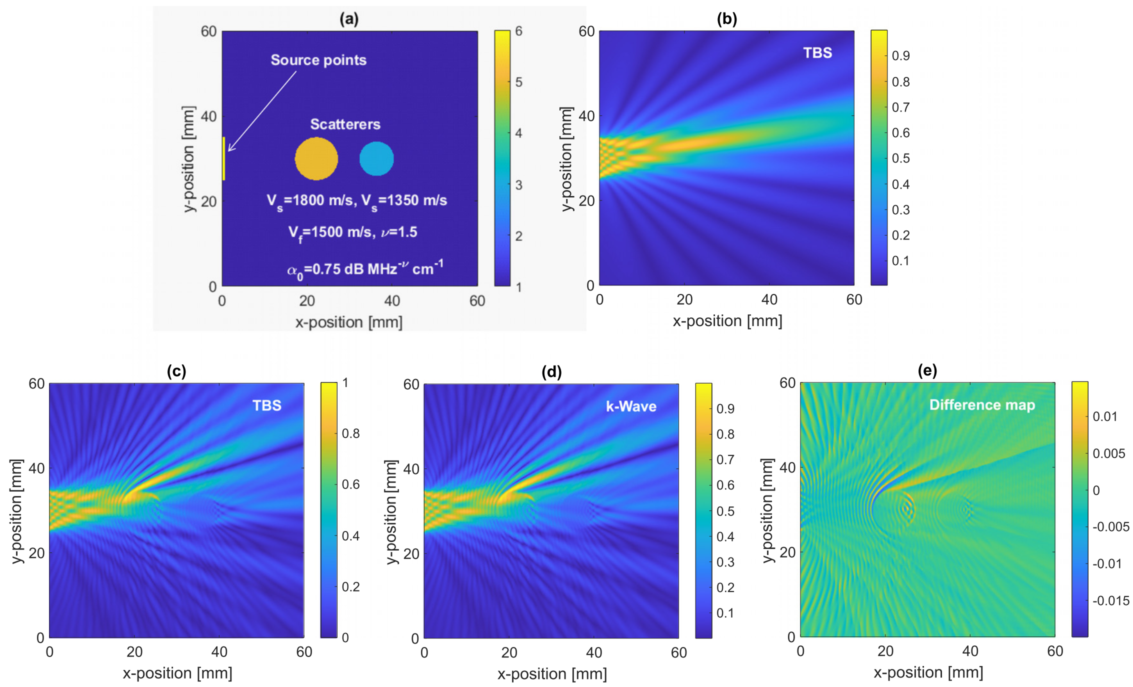

FIG. 6. (a) Simulation setup for a mixed medium (absorbing, dispersive, and scattering). (b) Demonstration of a steered beam (propagating through the absorbing and dispersive medium only). (c) and (d) Spatial distribution of pressure for the mixed medium, as shown in (a), generated using the TBS and K-WAVE methods, respectively. (e) Error map (difference between the TBS and K-WAVE results).

comparison. GPU accelerated numerical computations were carried out. Perfect agreement has been noticed between the TBS and K-WAVE results. The TBS method can provide a map of the pressure field within ~10 s for the computational domain considered in this study. The computation time for this approach is found to be 77× (average) faster than the latter. The TBS technique has emerged as a universal numerical method for accurate calculations of pressure field for all possible conditions associated with real tissue media.

SUPPLEMENTARY MATERIAL

See the supplementary material for the following results: (i) the actual pressure field (without normalization) produced by the TBS and K-WAVE methods; (ii) phase maps obtained using these techniques for the absorbing-dispersive medium corresponding to Fig. 3; (iii) the steady state pressure field distribution (both amplitude and phase) for an absorbing medium; (iv) same as (ii), but for an inhomogeneous medium corresponding to Fig. 4; and (v) the steady state spatial distribution of the normalized pressure amplitude and phase for the same linear array of sources for an inhomogeneous region with sound speeds $v_s = 1350$ m/s and $v_s = 1800$ m/s.

ACKNOWLEDGMENTS

The computational results reported in this work were performed on the Central Computing Facility of IIITA, Prayagraj. U.M. thanks the members of the Biomedical Imaging Laboratory for their support during this work and UGC NFSC [No. F. 82-44/2020 (SA-III)]. R.K.S. acknowledges the financial support received from ANRF (No. CRG/2023/003278). B.T.C. thanks EPSRC, UK, Grant Nos. EP/W029324/1 and EP/T014369/1.

AUTHOR DECLARATIONS

Conflict of interest

The authors have no conflicts to disclose.

DATA AVAILABILITY

The developed codes are available in GitHub (https://github.com/ratanksaha/Ultrasonic-field-calculation-2D). Generated data can be obtained from the authors upon request.

Anvari, A., Forsberg, F., and Samir, A. E. (**2015**). "A primer on the physical principles of tissue harmonic imaging," Radiographics **35**(7), 1955–1964.

Arfken, G. B., Weber, H. J., and Harris, F. E. (**1995**). *Mathematical Methods for Physicists* (Academic Press, New York).

Aubry, J.-F., Bates, O., Boehm, C., Butts Pauly, K., Christensen, D., Cueto, C., Gélat, P., Guasch, L., Jaros, J., Jing, Y., Jones, R., Li, N., Marty, P., Montanaro, H., Neufeld, E., Pichardo, S., Pinton, G., Pulkkinen, A., Stanziola, A., Thielscher, A., Treeby, B., and van 't Wout, E. (**2022**). "Benchmark problems for transcranial ultrasound simulation: Intercomparison of compressional wave models," J. Acoust. Soc. Am. **152**(2), 1003–1019.

Beyer, R. T. (**2008**). "The parameter B/A," in *Nonlinear Acoustics*, edited by M. F. Hamilton and D. T. Blackstock (Acoustical Society of America, Melville, NY), pp. 25–39.

Bojarski, N. N. (**1982**). "The *k*-space formulation of the scattering problem in the time domain," J. Acoust. Soc. Am. **72**(2), 570–584.

Born, M. (**1926**). "Quantenmechanik der stoßvorgänge" ("Quantum mechanics of collision processes"), Z. Phys. **38**(11–12), 803–827.

Bransden, B. H., and Joachain, C. J. (**2003**). *Physics of Atoms and Molecules*, 2nd ed. (Prentice Hall, Harlow, UK).

Chen, W., and Holm, S. (**2004**). "Fractional Laplacian time-space models for linear and nonlinear lossy media exhibiting arbitrary frequency power-law dependency," J. Acoust. Soc. Am. **115**(4), 1424–1430.

Christopher, P. T., and Parker, K. J. (**1991**). "New approaches to nonlinear diffractive field propagation," J. Acoust. Soc. Am. **90**(1), 488–499.

Colton, D., and Kress, R. (**1998**). *Inverse Acoustic and Electromagnetic Scattering Theory*, 2nd ed. (Springer, New York).

Demi, L., Verweij, M. D., de Jong, N., and van Dongen, K. W. A. (**2010**). "Modeling nonlinear medical ultrasound via a linearized contrast source method," in *Proceedings of the IEEE International Ultrasonics Symposium (IUS)*, San Diego, CA (IEEE, New York), pp. 2175–2178.

Eijkhout, V. (**2022**). "Parallel programming in MPI and OpenMP," 2nd ed., Vol. 2.

Gan, W. S. (**2021**). *Nonlinear Acoustical Imaging* (Springer, New York).

Garcia, D., and Varray, F. (**2024**). "SIMUS3: An open-source simulator for 3-D ultrasound imaging," Comput. Methods Programs Biomed. **250**, 108169.

Gu, J., and Jing, Y. (**2015**). "Modeling of wave propagation for medical ultrasound: A review," IEEE Trans. Ultrason. Ferroelectr. Freq. Control **62**(11), 1979–1993.

Gu, J., and Jing, Y. (**2021**). "mSOUND: An open source toolbox for modeling acoustic wave propagation in heterogeneous media," IEEE Trans. Ultrason. Ferroelectr. Freq. Control **68**(8), 1476–1486.

Hamilton, M. F., and Blackstock, D. T. (**1998**). *Nonlinear Acoustics* (Academic Press, New York).

Hill, C. R., Bamber, J. C., and ter Haar, G. R. (**2004**). *Physical Principles of Medical Ultrasonics* (John Wiley & Sons, Hoboken, NJ).

Jakobsen, M., Huang, X., and Wu, R.-S. (**2020a**). "Homotopy analysis of the Lippmann–Schwinger equation for seismic wavefield modelling in strongly scattering media," Geophys. J. Int. **222**(2), 743–753.

Jakobsen, M., Wu, R.-S., and Huang, X. (**2020b**). "Convergent scattering series solution of the inhomogeneous Helmholtz equation via renormalization group and homotopy continuation approaches," J. Comput. Phys. **409**, 109343.

Jensen, J. A. (**1991**). "A model for the propagation and scattering of ultrasound in tissue," J. Acoust. Soc. Am. **89**(1), 182–190.

Jing, Y., and Cleveland, R. O. (**2007**). "Modeling the propagation of nonlinear three-dimensional acoustic beams in inhomogeneous media," J. Acoust. Soc. Am. **122**(3), 1352–1364.

Kaltenbacher, B. (**2021**). "Periodic solutions and multiharmonic expansions for the Westervelt equation," Evol. Equations Control Theory **10**(2), 229–247.

Kaushik, A., Yalavarthy, P., and Saha, R. K. (**2020**). "Convergent born series improves the accuracy of numerical solution of time-independent photoacoustic wave equation," J. Mod. Opt. **67**(9), 849–855.

Krebes, E. S. (**2019**). *Seismic Wave Theory* (Cambridge University Press, Cambridge, UK).

Krüger, B., Brenner, T., and Kienle, A. (**2017**). "Solution of the inhomogeneous maxwell's equations using a Born series," Opt. Express **25**(21), 25165–25182.

Mandal, U., Singh, N., Singh, K., Hagone, V. N., Singh, J., Anand, A. S., Cox, B. T., and Saha, R. K. (**2025**). "Efficient implementations of a Born series for computing photoacoustic field from a collection of erythrocytes," Photoacoustics **43**, 100724.

Martin, E., Jaros, J., and Treeby, B. E. (**2020**). "Experimental validation of k-wave: Nonlinear wave propagation in layered, absorbing fluid media," IEEE Trans. Ultrason. Ferroelect. Freq. Control **67**(1), 81–91.

Mehtaj, N., and Banerjee, S. (**2025**). "Scientific machine learning for elastic and acoustic wave propagation: Neural operator and physics-guided neural network," Sensors **25**(12), 3588.

Morse, P. M., and Feshbach, H. (**1953**). *Methods of Theoretical Physics* (McGraw-Hill, New York), pp. 791–895.

Morse, P. M., and Ingard, K. U. (**1968**). *Theoretical Acoustics* (Princeton University Press, Princeton, NJ).

O'Donnell, M., Jaynes, E., and Miller, J. (**1981**). "Kramers–Kronig relationship between ultrasonic attenuation and phase velocity," J. Acoust. Soc. Am. **69**, 696–701.

Osnabrugge, G., Benedictus, M., and Vellekoop, I. M. (**2021**). "Ultra-thin boundary layer for high-accuracy simulations of light propagation," Opt. Express **29**(2), 1649–1658.

Osnabrugge, G., Leedumrongwatthanakun, S., and Vellekoop, I. M. (**2016**). "A convergent born series for solving the inhomogeneous Helmholtz equation in arbitrarily large media," J. Comput. Phys. **322**, 113–124.

Pinton, G. F., Trahey, G. E., and Dahl, J. J. (**2011**). "Sources of image degradation in fundamental and harmonic ultrasound imaging using nonlinear, full-wave simulations," IEEE Trans. Ultrason. Ferroelectr. Freq. Control **58**(4), 754–765.

Saha, R. K. (**2007**). "Some studies on approximate methods in acoustic scattering problems," Ph.D. thesis, West Bengal University of Technology, Kolkata, India.

Saha, R. K. (**2020**). "Numerical solution to the time-independent inhomogeneous photoacoustic wave equation using the Born series methods," J. Opt. Soc. Am. A **37**(12), 1907–1915.

Saha, R. K. (**2021**). "Solving time-independent inhomogeneous optoacoustic wave equation numerically with a modified Green's function approach," J. Acoust. Soc. Am. **149**(6), 4039–4048.

Saha, R. K. (**2025a**). "Photoacoustic field calculation," GitHub, https://github.com/ratanksaha/Photoacoustic-field-calculation.

Saha, R. K. (**2025b**). "Ultrasonic field calculation (2D)," GitHub, https://github.com/ratanksaha/Ultrasonic-field-calculation-2D.

Saha, R. K., and Sharma, S. K. (**2005**). "Validity of a modified born approximation for a pulsed plane wave in acoustic scattering problems," Phys. Med. Biol. **50**(12), 2823–2836.

Sai Ganesh, C. S., Jyothi, V. B. N., Aoutithiye Barathwaj, S. R. Y., and Azhagumurugan, R. (**2022**). "Machine learning based classification and modelling of underwater acoustic communication," in *Proceedings of OCEANS 2022—Chennai*, Chennai, India (IEEE, New York).

Sakurai, J. J. (**1967**). *Advanced Quantum Mechanics* (Addison-Wesley, Reading, MA).

Sanders, J., and Kandrot, E. (**2011**). *CUDA by Example: An Introduction to General-Purpose GPU Programming* (Addison-Wesley, Reading, MA).

Sharma, S. K., and Saha, R. K. (**2004**). "On the validity of some new acoustic scattering approximations," Waves Random Complex Medium **14**, 525–537.

Thoens-Zueva, A., Schmidt, K., and Semin, A. (**2017**). "Multiharmonic analysis for nonlinear acoustics with different scales," arXiv:1701.02097.

Treeby, B. E., and Cox, B. T. (**2010a**). "k-Wave: MATLAB toolbox for the simulation and reconstruction of photoacoustic wave fields," J. Biomed. Opt. **15**(2), 021314.

Treeby, B. E., and Cox, B. T. (**2010b**). "Modeling power law absorption and dispersion for acoustic propagation using the fractional Laplacian," J. Acoust. Soc. Am. **127**(5), 2741–2748.

Treeby, B. E., and Cox, B. T. (**2011**). "A *k*-space Green's function solution for acoustic initial value problems in homogeneous media with power law absorption," J. Acoust. Soc. Am. **129**(6), 3652–3660.

Treeby, B. E., Jaros, J., Rendell, A. P., and Cox, B. T. (**2012**). "Modeling nonlinear ultrasound propagation in heterogeneous media with power law absorption using a *k*-space pseudospectral method," J. Acoust. Soc. Am. **131**(6), 4324–4336.

van Manen, D., Robertsson, J. O. A., and Curtis, A. (**2005**). "Modeling of wave propagation in inhomogeneous media," Phys. Rev. Lett. **94**(16), 164301.

Varray, F., Basset, O., Cachard, C., Demi, L., van Dongen, K. W. A., and Verweij, M. D. (**2013**). "Nonlinear acoustic propagation simulation tools: Comparison of BBGASM and INCS up to the fifth harmonic component," in *Proceedings of the IEEE International Ultrasonics Symposium (IUS)*, Prague, Czech Republic (IEEE, New York), pp. 1033–1036.

Varray, F., Cachard, C., Ramalli, A., Tortoli, P., and Basset, O. (**2011**). "Simulation of ultrasound nonlinear propagation on GPU using a generalized angular spectrum method," J. Image Video Proc. **2011**, 17.

Varslot, T., and Taraldsen, G. (**2005**). "Computer simulation of forward wave propagation in soft tissue," IEEE Trans. Ultrason. Ferroelectr. Freq. Control **52**(9), 1473–1482.

Veerababu, D., and Ghosh, P. K. (**2025**). "Solving 2-D Helmholtz equation in the rectangular, circular, and elliptical domains using neural networks," J. Sound Vib. **607**, 119022.

Verweij, M. D., and Huijssen, J. (**2009**). "A filtered convolution method for the computation of acoustic wave fields in very large spatiotemporal domains," J. Acoust. Soc. Am. **125**(4), 1868–1878.

Wang, S., Hossack, J. A., and Klibanov, A. L. (**2020**). "From anatomy to functional and molecular biomarker imaging, and therapy: Ultrasound is safe, ultrafast, portable, and inexpensive," Invest. Radiol. **55**(9), 559–572.

Wu, J., Tu, K., Liang, L., Wang, S., Wang, Z., and Lv, G. (**2022**). "Fast calculation of acoustic field distribution for ultrasonic transducers using lookup table method," Appl. Sci. **12**(17), 8459.

Zemp, R. J., Tavakkoli, J., and Cobbold, R. S. (**2003**). "Modeling of nonlinear ultrasound propagation in tissue from array transducers," J. Acoust. Soc. Am. **113**(1), 139–152.

Graphics processing unit accelerated Helmholtz equation solver in two dimensions using the traditional Born series formulation for linear and nonlinear media in biomedical ultrasound

Ujjal Mandal[1], Jagpreet Singh[2], Ben T Cox[3], and Ratan K Saha[1]

[1]Department of Applied Sciences, Indian Institute of Information Technology Allahabad, Jhalwa, Prayagraj, 211015, Uttar Pradesh, India
[2]Department of Computer Science and Engineering, Indian Institute of Technology Ropar, Street 29, Ropar, 140001, Punjab, India
[3]Department of Medical Physics and Biomedical Engineering, University College London, Gower Street, London, WC1E 6BT, UK

Supplementary materials

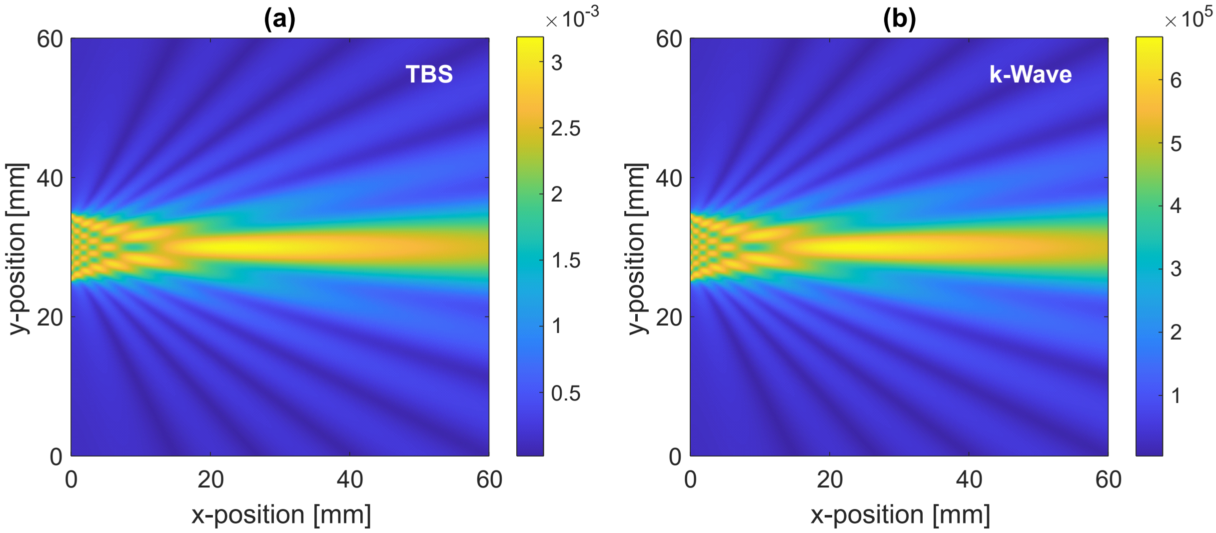

Figure S1: (a)-(b) Pressure field (in Pa) produced by the TBS and k-Wave methods, respectively. Here, we chose $|S| = 1000000$ Pa/m^2 for the TBS technique and source.p $= 1000000$ Pa for the k-Wave module.

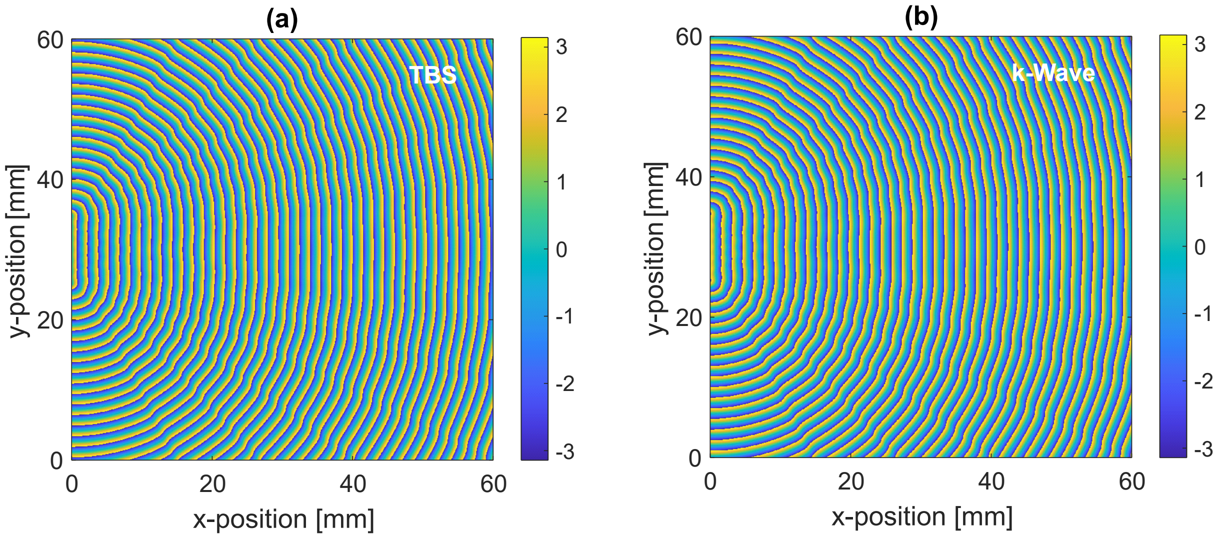

Figure S2: Phase maps for the TBS and k-Wave methods corresponding to Fig. 4.

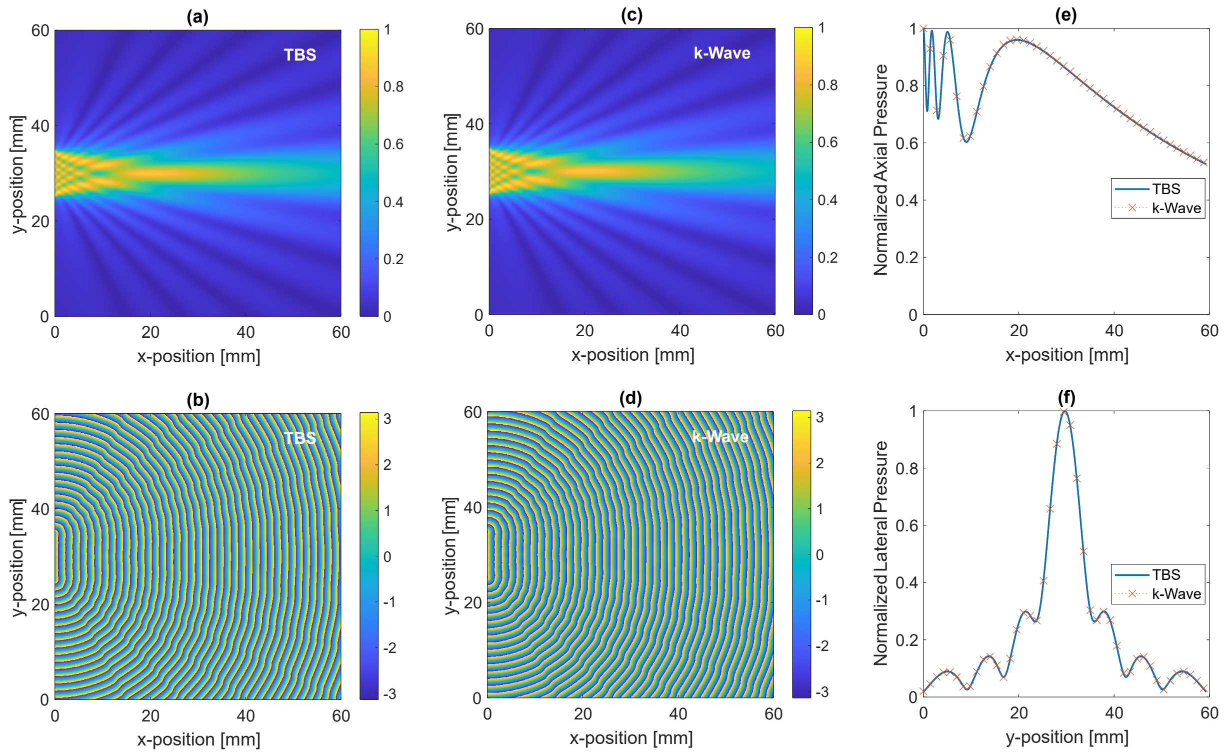

Figure S3: (a)-(b) Visualization of the steady state pressure field distribution (amplitude and phase) for the TBS scheme for an absorbing medium having $\alpha_0 = 5.5 \times 10^{-10}$ Np(rad/s)$^\nu$ m^{-1} and $\nu = 1.5$. (c)-(d) Same results for the k-Wave toolbox. On and off axes plots of pressure data are shown in (e) and (f), respectively. The lateral line is $x = 41$ mm away from the line source.

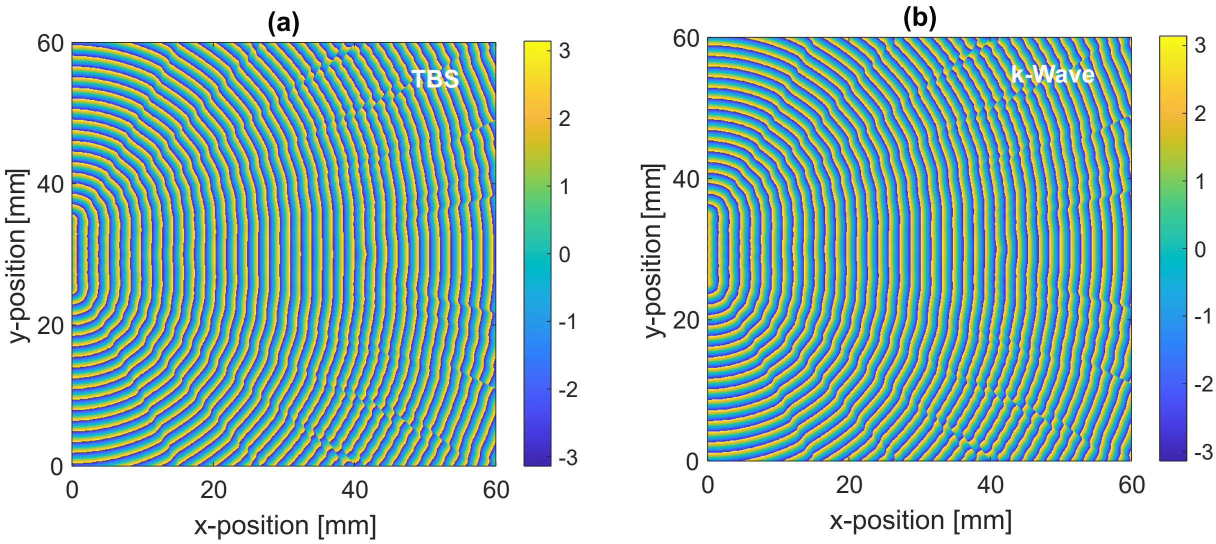

Figure S4: Phase plots for the TBS and k-Wave approaches corresponding to Fig. 5.

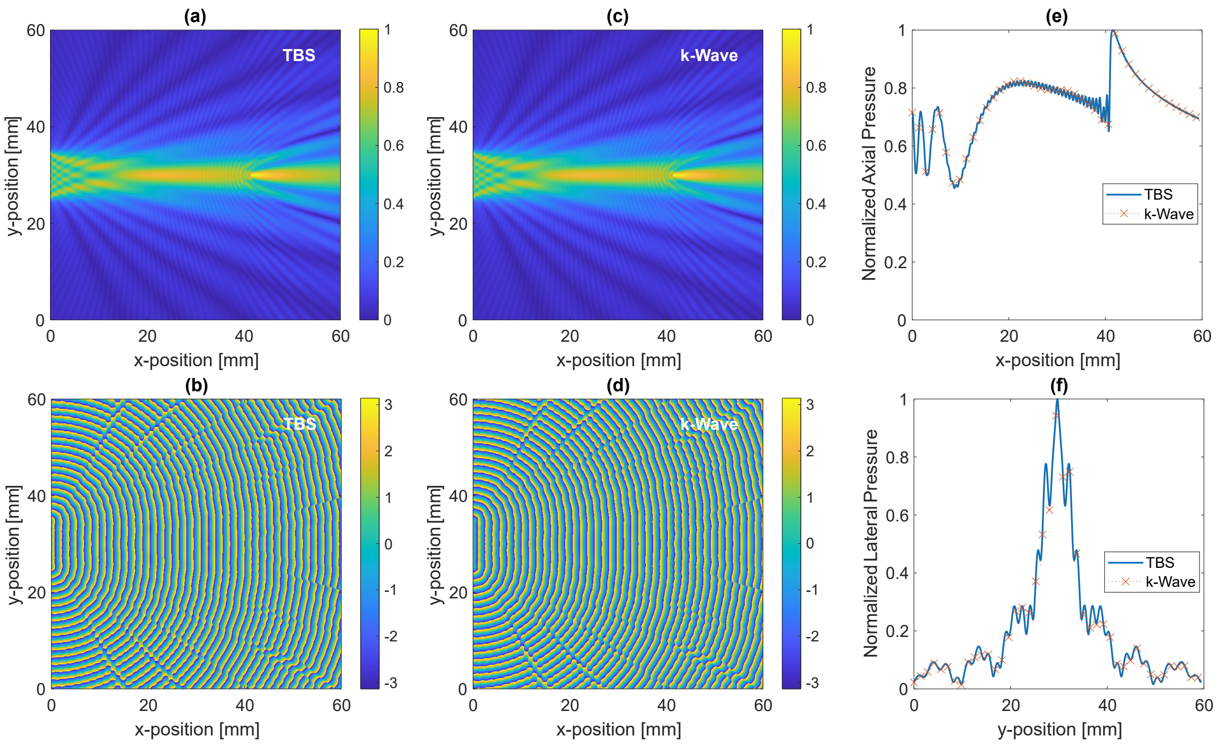

Figure S5: Same as S3 but for an inhomogeneous medium. The propagating medium contains an inhomogeneity of $a = 1$ mm with speed of sound $v_s = 1350$ m/s inside and $v_f = 1500$ m/s outside the scatterer.

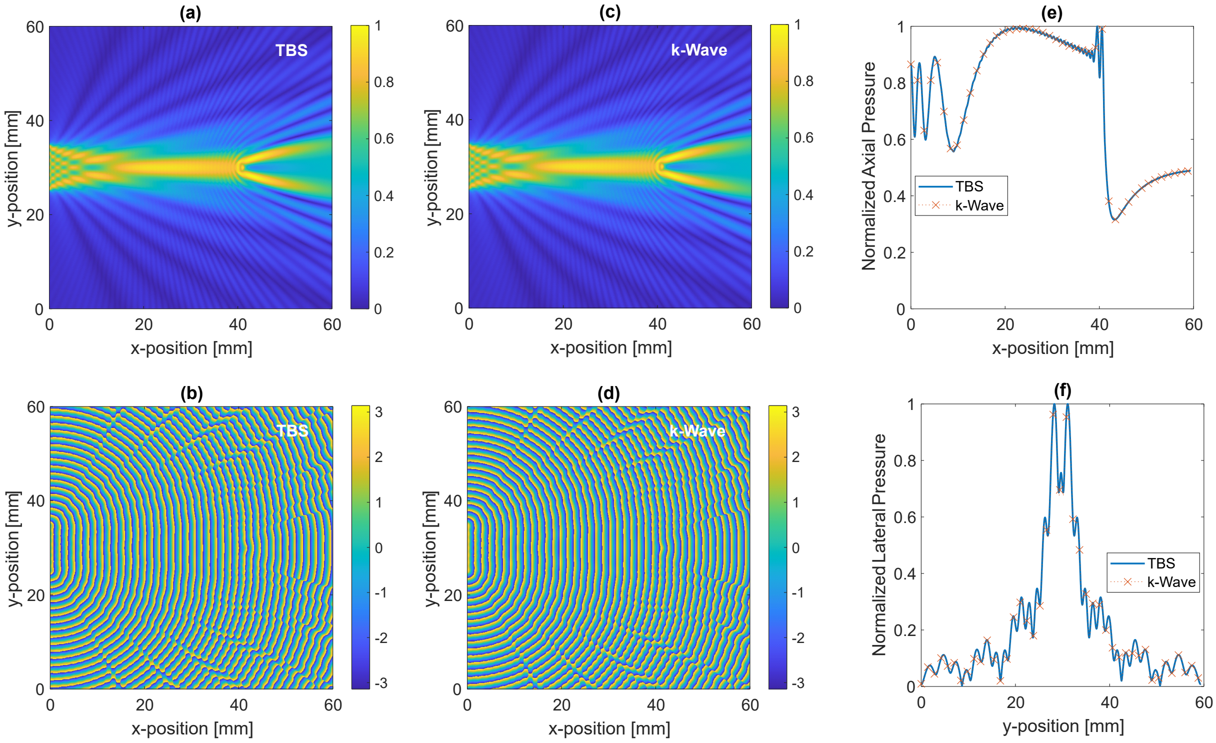

Figure S6: Same as Fig. S5 but for $v_s = 1800$ m/s

.